PHYSICAL REVIEW B **81**, 014111 (2010)

Strength effects in diamond under shock compression from 0.1 to 1 TPa

R. S. McWilliams,[1,2,*] J. H. Eggert,[2] D. G. Hicks,[2] D. K. Bradley,[2] P. M. Celliers,[2] D. K. Spaulding,[1] T. R. Boehly,[3] G. W. Collins,[2] and R. Jeanloz[1]

[1]*Department of Earth and Planetary Science, University of California–Berkeley, Berkeley, California 94720, USA*

[2]*Physics Division, Physical and Life Science Directorate, Lawrence Livermore National Laboratory, Livermore, California 94550, USA*

[3]*Laboratory for Laser Energetics, University of Rochester, Rochester, New York 14623, USA*

(Received 3 October 2009; published 22 January 2010)

A two-wave shock structure—elastic precursor followed by an inelastic compression wave—is observed in single crystal and polycrystalline diamond laser shock compressed to peak stresses as high as 800 GPa. The Hugoniot elastic limits are measured to be 80 (±12), 81 (±6), and 60 (±3) GPa for the ⟨100⟩, ⟨110⟩, and ⟨111⟩ orientations of single crystals with the directional dependence attributable to the relative increase in strength under confining stress. These values imply a single crystal yield strength approximately 1/3 of theoretical predictions. The measurements reveal clear deviations from an elastic-plastic response upon dynamic yielding with significant relaxation toward an isotropic stress state for shock stresses of at least 160 GPa. Previously reported signatures of melting at 700–800 GPa along the diamond Hugoniot may be related to the transition from a two-wave to a single-wave structure, supporting the interpretation that melting begins at lower stresses (~600 GPa) with the appearance of an optically reflecting phase of carbon.

DOI: 10.1103/PhysRevB.81.014111 PACS number(s): 62.50.Ef, 91.60.Gf, 91.60.Fe

I. INTRODUCTION

Diamond has the largest resistance to deformation of any known bulk material; it is of unparalleled utility in numerous technological applications, due also to its transparency, chemical inertness and high thermal conductivity, and many have sought to predict or measure it's yield strength.[1–11] In the present study, we characterize its yielding by measuring the behavior of single-crystal and polycrystalline diamond under compression by large-amplitude shock waves between 100 and 1000 GPa.

In solids, minimum elastic energy is obtained under hydrostatic (isotropic) stress conditions.[12] When stressed anisotropically, a solid material may behave macroscopically as a fluid with stress relaxing toward hydrostatic conditions; or the material can resist yielding, sustaining anisotropic stress through strength effects. Strength is manifested in numerous ways under dynamic loading of solids, the most conspicuous being the Hugoniot elastic limit (HEL): the stress below which strain is purely elastic and above which significant inelastic yielding occurs. Compression to stresses just beyond the HEL is associated with the formation of a two-wave shock structure, featuring an elastic precursor traveling at a longitudinal sound speed (and compressing the material to near its HEL) followed by an inelastic wave that achieves the peak compression.

Because the stress of the precursor shock represents the limit of elastic deformation, it provides a measure of the material's initial yield strength. For the inelastic wave, the effects of strength in general depend on material, shock amplitude, strain rate, and time.[13–21] The *elastic-plastic* model,[13] for example, assumes that strength is maintained during inelastic deformation with deviatoric stress magnitudes comparable to those observed at the HEL. Alternatively, the *elastic-isotropic* model[14] assumes that strength is lost during inelastic compression, resulting in shock-compressed states of hydrostatic stress. The behavior of real materials falls between these two extremes, for compression just beyond the HEL.

Materials exhibiting a total or partial loss of strength during inelastic compression tend to be brittle and characterized by high strength and low thermal conductivity at ambient conditions, e.g., the dielectrics quartz (SiO_2),[17,22,23] boron carbide (B_4C),[19,20] periclase,[15,17] and corundum (Al_2O_3).[14,17,24] The prevailing explanation for strength loss under dynamic yielding is that inelastic deformation is localized in shear bands, where elevated local temperatures can transiently enhance slip, in some cases through melting.[15–18] Thermal-strain localization is counterbalanced by heat conduction and hence is favored in thermally resistive materials. That strength loss occurs most prevalently in brittle solids also suggests a connection with brittle fracture. Metals, with low strength, high thermal conductivity and typically ductile yielding, tend toward elastic-plastic responses.

Diamond, a brittle dielectric of uniquely high strength and thermal conductivity, lacks an obvious analog among other solids that have been studied with shock compression. High-strength, high thermal-conductivity moissanite (SiC) may be the closest and resembles an elastic-plastic material under shock loading.[19,20] However, silicon (Si)—which also has high strength and high thermal conductivity and is isostructural with diamond—behaves as an elastic-isotropic material.[25] While diamond's resistance to plastic flow and tendency to yield by fracturing at ambient pressure and temperature is well known,[26] plastic flow has been observed in diamond at high pressures[8] and temperatures[26] (though on significantly longer time scales than are explored by shock compression). In the present study, we find that the response of diamond to shock loading ranges from nearly elastic-isotropic to nearly elastic-plastic, correlated with initial sample properties.

The response of diamond to dynamic compression has been measured previously[11,27–36] although the low-stress shock-compression regime (<600 GPa), where strength ef-

fects should play the largest role, has received relatively little attention.[11,27–30] Early equation-of-state measurements at 100–600 GPa reported a single-wave structure.[27] Subsequent measurements, however, documented elastic precursor waves at 180–250 GPa.[28,30] The present results are consistent with the latter studies.

Recent shock experiments on diamond have focused on higher stresses, 500–3500 GPa.[31–36] Melting has been found to initiate at 600–800 GPa[31,33,35–38] and most shock equation-of-state measurements have documented stresses near or above this stress.[32–35] Whereas the occurrence of melting suggests that strength should not play a role in this stress regime, the present observations reveal that this is not the case. Also, recent ramp-wave loading experiments indicate that solid diamond exhibits significant strength to ramp stresses of ~800 GPa,[11] raising the possibility that strength can similarly influence the shock-wave response.

II. MATERIALS AND EXPERIMENTAL METHOD

Single-crystal diamond samples were cut for shock propagation in the three crystallographic orientations that exhibit ideal uniaxial strain for elastic shock compression:[39,40] ⟨100⟩, ⟨110⟩, and ⟨111⟩. The ⟨100⟩ (type Ia) and ⟨110⟩ (types Ia and IIa) samples were transparent, colorless, and inclusion free, and were fashioned into polished circular disks 100–500 μm in thickness and 1 mm in diameter; these were supplied by Delaware Diamond Knives, Inc. and Harris Diamond Co. The ⟨111⟩ samples were inclusion-free type Ib diamonds, transparent and yellow in color, cut into 1-mm-sided squares ~200 μm thick, with the broad surfaces formed by cleavage along {111} planes; these were supplied by Almax Industries. In some high-stress experiments, a microcrystalline synthetic (CVD) diamond was studied; this variety of polycrystal, supplied by Diamond Materials GmbH, has been studied previously under dynamic compression.[11,35,36]

The targets consisted of diamond mounted on a diamond-turned (optically finished) 1100 aluminum buffer (Aero Research Associates, Inc.), 50–100 μm thick, with 8–20 μm of plastic ablator (CH) deposited on the opposite surface (Fig. 1). In most targets, a 137-μm-thick, z-cut quartz window (Meller Optics, Inc.) was placed adjacent to the diamond as a reference standard. In some targets, two ~100-μm-thick diamonds of identical orientation were stacked with a 100 nm layer of aluminum deposited on a section of the interface between them to provide an internal surface at which to observe shock arrival in diamond (Fig. 2). Target components were aligned, stacked with Norland-63 UV-cure photopolymer glue between parts, and compressed using a Fineplacer Pico (Finetech GmbH); targets were UV cured while under compression, reducing gaps between parts to a minimum.

A Wyco optical surface profilometer (Veeco Instruments) was used to create a two-dimensional thickness map of samples and targets throughout target assembly. Interference fringes observed in gaps between parts under illumination by white light, in combination with optical profilometry, were used to characterize gap thicknesses throughout the assembled targets. Targets with gap thicknesses exceeding ~1 μm were discarded because for larger thicknesses shock reverberation in the gap causes a significant perturbation in shock travel time. The 100-nm aluminum layer in the interface of stacked diamonds does not significantly affect our measurements. In some ⟨111⟩ samples, cleavage on different {111} planes resulted in a series of steps on diamond surfaces; care was taken to ensure that these steps did not interfere with the measurements.

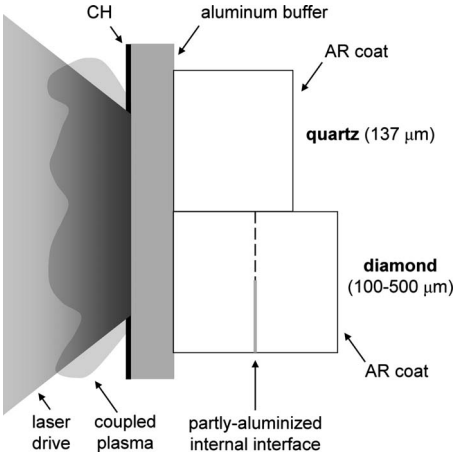

FIG. 1. Target schematic with the laser (left) incident on an ablative layer of polymer (CH), driving a shock through an Al buffer and into the diamond sample. In most cases, a z-cut quartz reference was placed on the buffer, adjacent to the diamond. In some cases, two diamonds were stacked on each other, effectively forming a single diamond with an internal interface, which was partially coated with ~100 nm of Al. An AR coating was sometimes used on the quartz and diamond free surfaces to permit observation of weakly reflecting shocks in the transparent samples. Line-imaging VISAR and SOP diagnostics view the target from the right. Targets are in an evacuated chamber for the experiment.

Shock waves were driven into the targets using two laser systems, Janus (100 GW at 532 nm) at Lawrence Livermore National Laboratory and Omega (3 TW at 355 nm) at the University of Rochester's Laboratory for Laser Energetics. One-dimensional loading and unloading was achieved by smoothing the drive laser foci with phase plate technology that provided uniform irradiation over a square region 1000 μm on a side, or a circular region 650 μm in diameter. This uniform, high-intensity laser ablated the target surface generating a high velocity plasma. In response to this large impulse, a planar shock having the dimension of the focal spot is generated in the target. As the shock propagates across the target, lateral unloading reduces the diameter of the planar region to between 950 and 100 μm, depending on shock-propagation distance, the phase plate used and—for the square plate—the plate orientation relative to the target. The size and quality of the planar region was documented by the observed uniformity of shock-arrival times at a given depth in the target.

Pulses of 1–6 ns duration were used. The 6 ns pulses provide an optimum degree of shock steadiness during the experiment (quasisteady loading) but with a limited peak stress; whereas 1–4 ns pulses typically create higher peak

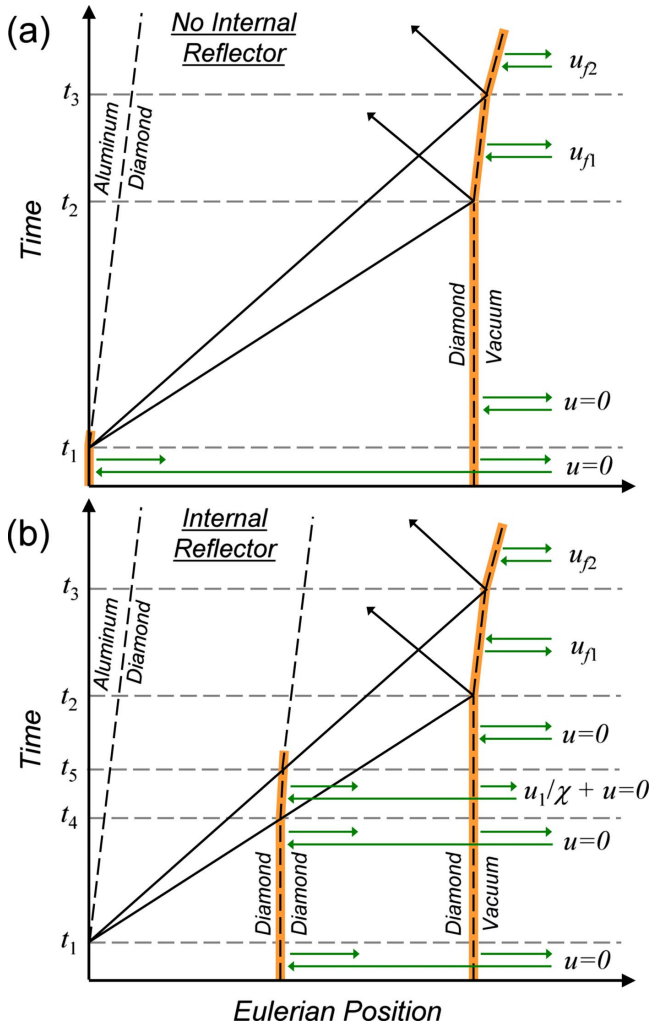

FIG. 2. (Color online) Position vs time diagrams illustrating quasisteady shock experiments in diamond: (a) VISAR views the base of the diamond, Figs. 3(a) and 3(c) and (b) VISAR views a reflecting internal interface, Fig. 3(c) only. Shocks and rarefactions (solid black lines) are presumed to be discontinuities and dashed black lines and dashed gray lines indicate boundaries in the target and timing markers, respectively. Reflecting surfaces are indicated by orange highlighting; and green arrows are incident and reflected VISAR light (artificially offset in time for clarity) identifying the surfaces probed, and are labeled with the observed velocities.

stresses but result in shock decay with propagation distance due to unloading following shutoff of the laser drive. Characterization of loading stability is discussed in Appendix A.

Two line-imaging velocity interferometer (VISAR) systems were used to measure velocities and shock travel times.[41,42] The interferometric measurement of velocity by VISAR is given by

$$\text{Velocity} = \phi\left[\frac{\lambda}{2\tau(1+\delta)\chi}\right]. \quad (1)$$

The second term on the right (velocity per fringe, VPF) involves the wavelength of the VISAR probe laser ($\lambda = 532$ nm), the optical delay time τ introduced by the etalon in one leg of the interferometer, a correction $(1+\delta)$ for optical dispersion in the etalon, and a factor χ accounting for index of refraction effects in the shocked target. The first term $\phi = \phi' + b$ is the fringe shift (in counts), where ϕ' is the fractional fringe count relative to the initial (zero-velocity) phase, and b is an integer. The optical delay τ used in each VISAR channel was different, allowing the quantity b for each channel to be unambiguously resolved.[42] The values of χ varied with both spatial coordinate and time in a given VISAR record, and are summarized in Table I. VPF values are reported assuming $\chi = 1$.

TABLE I. VISAR index of refraction corrections.

Reflecting surface	χ
Quartz	
Interface behind shock	1.16 ± 0.04[a]
Reflecting shock front	1.546[b]
Free surface	1
Diamond	
Interface behind shock	…[c]
Reflecting shock front	2.424[d]
Free surface	1

[a]Reference 47.
[b]Reference 46.
[c]Optical correction not known, $\chi = 1$ assumed.
[d]Reference 31.

In the present experiments, interferometric velocity measurements were made of reflecting interfaces behind transparent shock fronts (giving particle velocity), of reflecting shock fronts (giving shock velocity), and of reflecting free surfaces of samples (giving free-surface velocity). Shock velocity was also measured from the timing of shock arrival at various interfaces in the targets; arrivals were identified by changes in fringe phase and/or amplitude in the VISAR. A line-imaging streak optical pyrometer[43,44] (SOP) provided time-resolved thermal-emission data from the targets during most experiments.

The three streak cameras used in the VISAR and SOP were Hamamatsu C7700–01 models at Janus facility and were custom built at the Omega facility. Streak images of 10–40 ns duration were used and time resolution—including the effects of streak duration, slit width, and etalons—varied for each data set but was ~0.1 ns. Sweep-rate variations with time were measured and accounted for. At ambient conditions, diamond and quartz are transparent at the wavelengths used by these diagnostics.

Orientations of diamond single crystals were assumed to be those requested from the suppliers; deviations from ideal orientation are estimated as follows. In the case of ⟨111⟩ samples, distinct {111} cleavage planes allowed direct measurement (via optical profilometry) of the angle between crystallographic orientation and the bulk surface normal that defined the shock propagation direction; this angle was $\frac{1}{4}^\circ$ or less for all ⟨111⟩ samples. In the case of ⟨100⟩ and ⟨110⟩ samples, this angle was estimated from the parallelism of opposing surfaces, assuming one surface was of correct ori-

entation and the other of incorrect orientation. For the maximum thickness variation over a 1 mm diameter observed in these diamonds (5 μm), a $\sim\frac{1}{3}^\circ$ misalignment would be suggested; thus it is likely that the shock-propagation direction lies within $\sim 1^\circ$ of the $\langle 100\rangle$ and $\langle 110\rangle$ orientations. The densities of the diamond, quartz, and aluminum samples were taken to be 3.52, 2.65, and 2.71 g/cc, respectively.

For experiments in which shock fronts in quartz[45] or diamond[31] were reflecting, antireflection (AR) coatings were sometimes used on free surfaces; this was necessary to observe shock fronts with weak ($<10\%$) reflectivities using VISAR. When AR coatings were used, the free surface became reflecting on shock arrival and its subsequent velocity could be measured.

The quartz window acts as a reference for determining the shock conditions in the aluminum buffer and the diamond. In the majority of our experiments, quartz was shocked into the molten regime and the shock front was reflecting and emissive, permitting time-resolved measurement of shock velocity using VISAR, and thermal emission using SOP.[45,46] This data was used to document the stability of the laser drive during the experiment (Appendix A). In some cases a poor AR coating prevented direct observation of the reflecting shock with VISAR; shock velocity was determined in such cases from the transit time of the shock across the quartz; time-resolved thermal emission was still observed. For a single experiment at the lowest stress studied here, shocked quartz was transparent to VISAR and the velocity of the quartz-aluminum interface was measured.[47] Preheating due to the laser drive at the maximum laser energies studied here has been previously found to be negligible in these types of targets.[48]

III. ANALYSIS AND RESULTS

Shock conditions were assessed using the Rankine-Hugoniot equations that relate shock-wave velocity D, particle velocity u, density ρ (or volume $V=1/\rho$), and longitudinal shock stress P through conservation of (linear) momentum and mass[22]

$$P_b = P_a + \rho_a(D_b - u_a)(u_b - u_a), \tag{2}$$

$$\rho_b = \rho_a \frac{D_b - u_a}{D_b - u_b}. \tag{3}$$

Subscript a indicates conditions ahead of the shock front, and subscript b is used to denote shock velocity (D_b) and the conditions behind the shock. For a two-wave system, these equations are applied successively to the first and second shocks. The preshock state of the system is $u_0=0$, $P_0=0$, and ρ_0 (ambient density), and states behind the first and second waves (traveling at D_1 and D_2) are u_1, P_1, and ρ_1 and u_2, P_2, and ρ_2, respectively.

The P-ρ-D-u states obtained in this manner define the shock Hugoniots of diamond, the loci of states achieved by shock compression from a particular initial state. In the present study, this initial state was varied by altering the properties of the diamond samples (e.g., the orientation of single crystals). The shock front is optically reflective for Hugoniot states above 600 GPa (Ref. 31) and these results are discussed separately from the experimental observations at stresses below 600 GPa. Steady-loading behavior is assumed in the analysis of our low-stress experiments because this is a good assumption in most cases (Appendix A).

A. Low-stress results

1. Observations

A two-wave structure was observed in all experiments below 600 GPa (Figs. 2 and 3). Free-surface velocity profiles (Fig. 4) show features common to elastic-inelastic two-wave shock structures[16,17,22,49–51] with the leading elastic shock consisting of a sharp jump in free-surface velocity u_f, followed by u_f decreasing with time prior to second-wave arrival. On second-wave arrival, the profile varies depending on sample orientation and driving stress, the second-wave arrival generally being sharper at higher peak stress and more distended at lower stress. For $P_2=200-300$ GPa in the $\langle 100\rangle$ and $\langle 110\rangle$ orientations, the second-shock arrival features a sharp initial jump in velocity followed by a slow rise to peak velocity. This initial jump, observed previously in $\langle 110\rangle$ diamond,[30] is due to the interaction of the two-wave structure with the sample surface (Fig. 5).[13,25,50] The jump leading the second-wave arrival is slightly larger than the jump observed on first-shock arrival as is commonly observed when the sample surface is unconfined.[13,50]

In our analysis, we make use of the observation that the first wave is transparent to VISAR interferometry and the second is nontransparent to VISAR (Fig. 3). This is consistent with identification of the first wave as elastic and the second as inelastic, with scattering from heterogeneous damage the likely cause of transparency loss.

2. Measurement of first-wave conditions

The particle velocity u_1 is obtained from the free-surface velocity following arrival of the first shock, u_{f1}, assuming $u_{f1}=2u_1$.[14,22,23,28] Uncertainty is estimated from the full range of velocities observed between first- and second-wave arrivals at the free surface.

Shock velocity D_1 is determined from travel time across the diamond. The measured D_1 are comparable to the ambient longitudinal sound speeds in the $\langle 100\rangle$, $\langle 110\rangle$, and $\langle 111\rangle$ orientations (17.53, 18.32, and 18.58 km/s, respectively).[39,52] This is additional evidence that the first wave is elastic. D_1 appears to decrease somewhat between the first and second diamond of stacked targets by ~ 1 km/s,[47] presumably as a result of stress relaxation behind the precursor;[51] because the change in velocity is on the order of the absolute measurement uncertainty, the average is used for D_1. The stress P_1 and density ρ_1 are then determined through Eqs. (2) and (3).

3. Measurement of second-wave conditions

Shock velocity D_2 is determined from shock travel time, using shock arrival at the free surface, and for stacked targets, arrival at the internal interface (in which case the two measurements are averaged). The effect of the precursor on

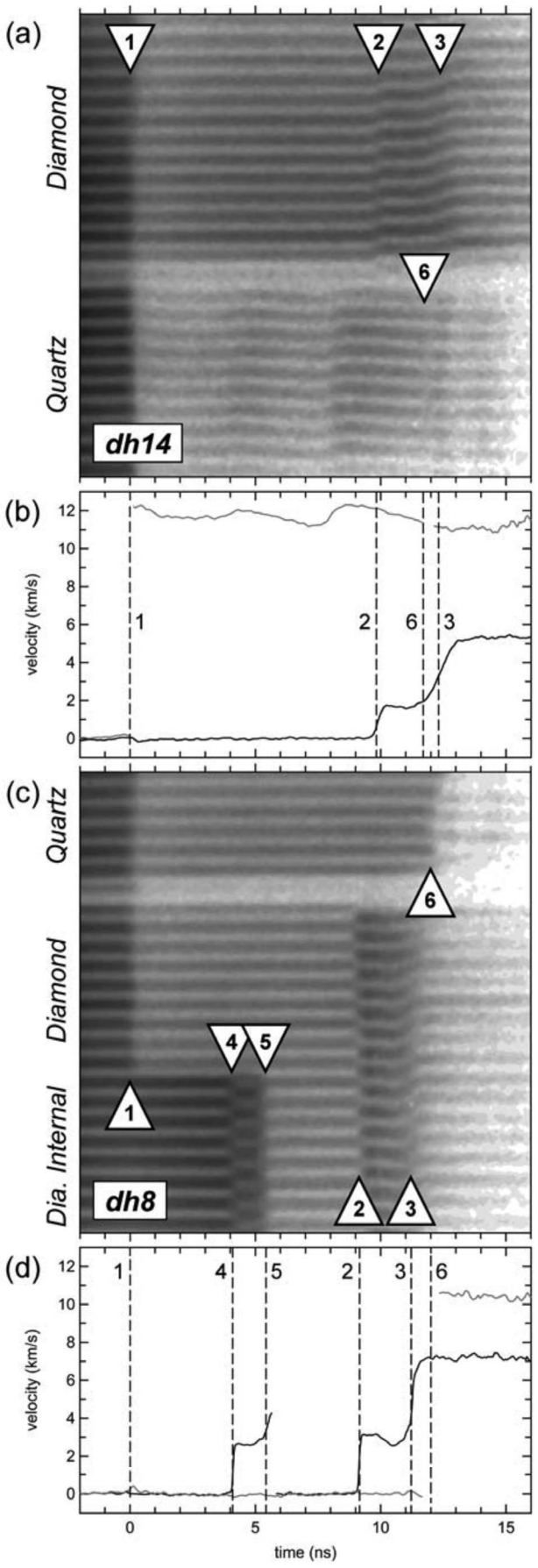

FIG. 3. Line VISAR [(a) and (c)] and resulting velocity records [(b) and (d)] for shots dh14 and dh8, respectively. Spatial (vertical) axes of (a) and (c) are 925 μm full scale and are labeled to indicate the target region: quartz, diamond, and diamond with a reflecting (Al-coated) internal interface. In (a) and (c), darker interference fringes correspond to higher reflection from the target. In plots (b) and (d), velocities for diamond and quartz are solid black and gray lines, respectively. Time zero corresponds to shock breakout into diamond and quartz. Events, numbered as in Fig. 2, are determined from changes in fringe phase ($\Delta\phi$) or intensity; the subsequent phase (ϕ) is determined from $\phi=0$ corresponding to a motionless surface. (1) Shock breakout from aluminum buffer, diamond and quartz rendered nontransparent and reflection from the buffer ceases; a reflecting shock is visible in quartz in (a) due to good AR coating on the quartz window ($\Delta\phi>0$ and $\phi>0$); for quartz in (c), and diamond in both targets, only an intensity drop is registered ($\Delta\phi=0$ and $\phi=0$). [(2) and (3)] Arrival of elastic and inelastic waves (respectively) at diamond free surface ($\Delta\phi>0$ and $\phi>0$). (4) Arrival of elastic wave at internal reflecting interface, wave is transparent ($\Delta\phi>0$ and $\phi>0$). (5) Arrival of inelastic wave at internal reflecting interface, wave is nontransparent ($\Delta\phi<0$ and $\phi=0$) (6) Arrival of shock at quartz free surface (character depends on the initial quality of the AR coating); subsequent to this event only free-surface reflection is observed with $\phi>0$. For the observed fringe shift at event 4, $\chi=1$ is assumed in reducing the data, and overlapping $\phi=0$ fringes from the free surface are subtracted. For both (a) and (c), the apparent VPF (for $\chi=1$) is 6.221 km/s per fringe shift. In selecting arrival times to determine shock velocity, arrival 1 is identified by the drop in fringe intensity; arrivals 2 and 4 are identified by sharp fringe shifts; arrival 3 is identified as the point of maximum free-surface acceleration; arrival 5 is identified by a sudden drop in fringe intensity and an incomplete fringe shift; and arrival 6 is identified by a fringe shift or an intensity drop. Arrival times are obtained self-consistently, accounting for the time resolution of the VISAR.

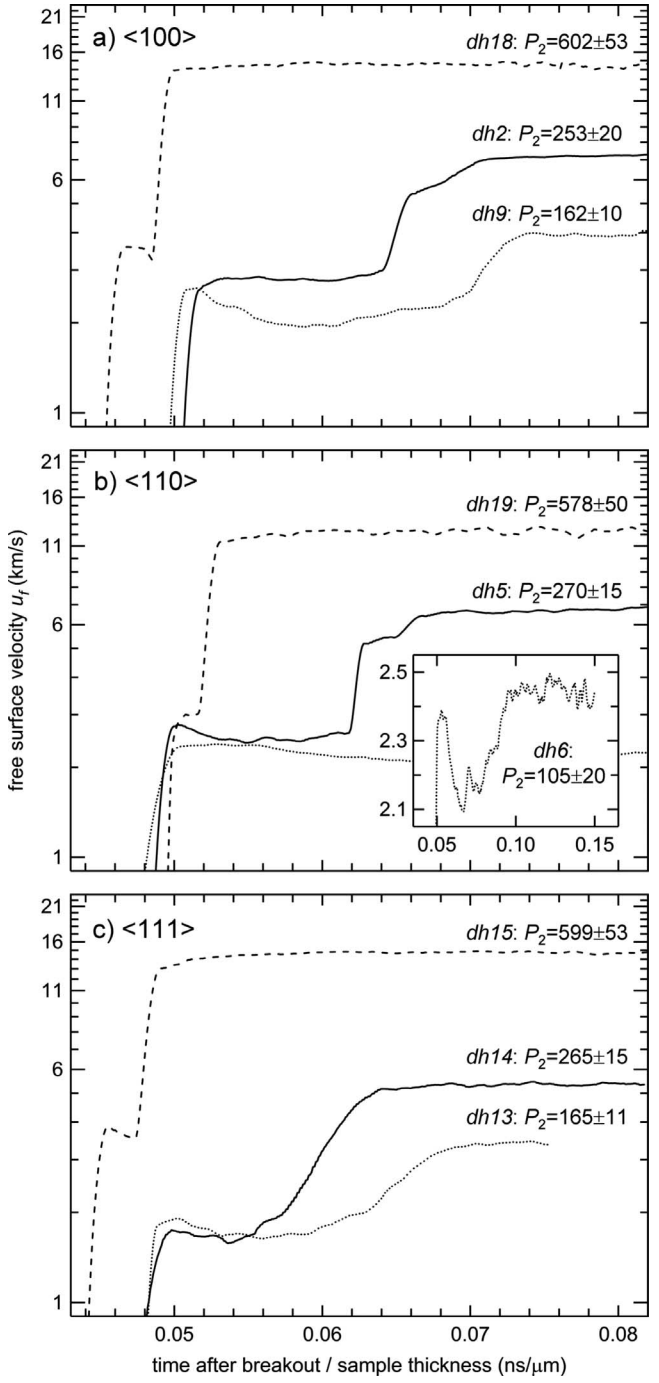

FIG. 4. Profiles of free-surface velocity u_f vs normalized time (time after the shock enters the diamond divided by the thickness of the diamond or diamond stack), for orientations (a) ⟨100⟩, (b) ⟨110⟩, and (c) ⟨111⟩. Normalization to diamond thickness results in identical arrival times for waves traveling at the same velocity. Inset in (b) is a detail (with a longer time scale) on the lowest amplitude wave in that figure.

velocity measurement at the internal interface is straightforward.

At the free surface, the effect of the prior arrival of the precursor is more complicated as reverberation between the free-surface release of the precursor and the approaching inelastic wave must be considered (Fig. 5).[14,22,50,53,54] We use

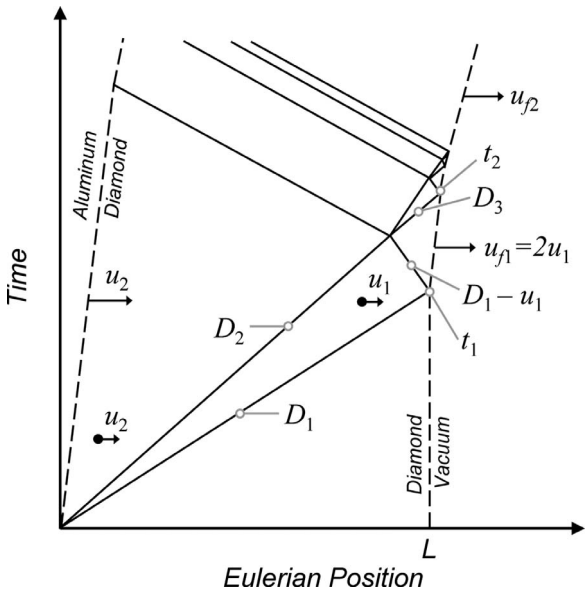

FIG. 5. Distance-time plot of reverberations following arrival of the elastic precursor at the free surface, after Refs. 53 and 54. Solid lines are shocks and rarefactions (labeled with Eulerian wave velocities) and dashed lines are material interfaces. Rarefactions are approximated as discontinuous waves.

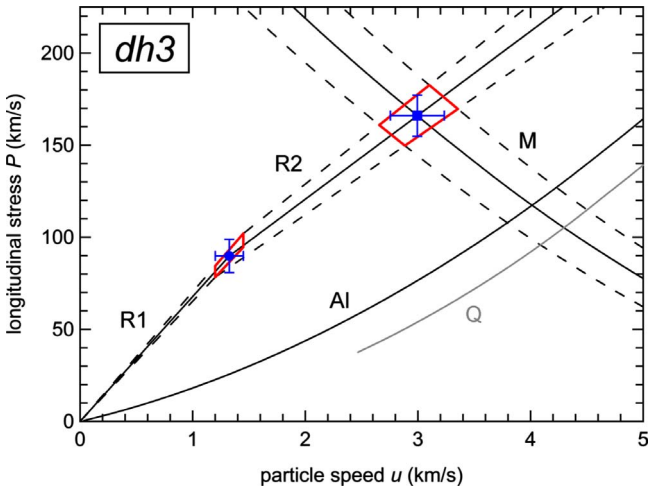

FIG. 6. (Color online) Impedance-match method for a representative experiment (dh3). The path to the first state in diamond is indicated by Rayleigh line R1 with a slope $\rho_0 D_1$ and the path from the first to the second state is indicated by Rayleigh line R2 with a slope $\rho_1(D_2-u_1)$. The aluminum Hugoniot (Al) is reflected (M) about the initial state in aluminum, intersecting with R2 and the quartz Hugoniot (Q), to estimate the release (into quartz) and reshock (into diamond) response of Al (Ref. 57); errors due to the reflected-Hugoniot approximation are negligible. Impedance matching was accomplished by first determining aluminum conditions from measured quartz conditions, then determining second-wave diamond conditions from aluminum conditions. Dashed lines indicate uncertainty in R1, R2, and M. Uncertainties in first- and second-wave states are represented in two ways: by orthogonal error bars (blue) and by polygonal zones (red), where the latter show covariance; orthogonal uncertainties are reported in Table II; polygonal uncertainties are shown in subsequent graphs when appropriate.

the reverberation treatment[53,54] with D_2 defined as

$$D_2 = \frac{(t_2 - t_1)(2D_1u_1 - 2u_1^2 - D_3D_1 + D_3u_1) + L(D_1 - u_1 + D_3)}{t_2(D_3 - 2u_1) + t_1(u_1 + D_1)} \tag{4}$$

where L is the diamond thickness (the total thickness in the case of stacked targets), t_1 is the transit time of the first wave across the diamond(s), t_2 is the apparent transit time of the second wave, and D_3 is the velocity of the wave that emerges from the interaction between the precursor release wave and the oncoming second shock. The quantity D_3 is not well known. One common assumption is that $D_3=D_1+2u_1$, which assumes that diamond is restressed to support a new elastic wave with the same velocity as the first.[14,22,53,54] This assumption seems realistic for the experiments on ⟨100⟩ and ⟨110⟩ diamond where the second-wave free-surface arrival event contains a clear elastic reverberation. However, it was observed in experiments on quartz[22,53] that this assumption produces unrealistic values of D_2 and that more reasonable results are obtained by assuming D_3 is significantly slower with a velocity closer to the bulk wave speed.

In the present study, we measured D_3 by comparing D_2 measured in the first diamond of stacked targets with that estimated using Eq. (4). The value of D_3 giving the best agreement between the two measurements is 82 (±5)% of D_1+2u_1 for P_2 between 150 and 300 GPa, consistent with the lower D_3 suggested by previous studies. We considered a systematic uncertainty of $(D_1+2u_1)>D_3>(D_2+2u_1)$ in applying Eq. (4) to all measurements, where the lower bound reproduces the slower measured value. At $P_2<200$ GPa, the shock velocity obtained from Eq. (4) is imprecise due to the long time between reverberations and the systematic uncertainty in D_3.

The particle velocity u_2, stress P_2, and density ρ_2 behind the second wave were determined simultaneously through impedance matching[22] using the Hugoniots of quartz[46,55] and aluminum,[56,57] the measured shock conditions in the quartz, the precursor shock conditions, and D_2 (Fig. 6). The shocks in quartz and aluminum consist of single waves at the conditions studied here.

Note that we observe $u_{f2}/u_2<2$ at $P_2<300$ GPa (Table II). For example, for $P_2=200-300$ GPa in the present study, u_{f2}/u_2 ratios of 1.69 (±0.12), 1.56 (±0.09), and 1.21 (±0.09) are observed for the ⟨100⟩, ⟨110⟩, and ⟨111⟩ orientations, respectively. Also, $u_{f2}/u_2\sim1.7$ has been reported for $P_2\sim200$ GPa in nearly ⟨111⟩-oriented diamond.[28] Such deviations from the frequently assumed $u_{f2}/u_2=2$ behavior[23,25,50,54] are likely due to strength effects and preclude the use of the free-surface release velocity to estimate u_2 in these low-stress experiments.

4. Hugoniot data and uncertainty

Hugoniot data at low stress (Table II) are plotted in Figs. 7 and 8, together with previous Hugoniot data in this stress regime on nearly ⟨111⟩-oriented diamond[28] (plotted with our ⟨111⟩ data) and ⟨100⟩ diamond.[27]

Uncertainties in the measured quantities—D_1, u_1, D_2, and the quartz shock velocity D_Q—were propagated to dependant quantities—e.g. P_1, ρ_1, u_2, P_2, and ρ_2—with careful consideration of covariance. To represent covariance in the uncertainty of dependant quantities graphically, polygonal bounding regions are used (rather than orthogonal error bars) as shown in Figs. 6–8. These contain all solutions to the analysis that fall within the uncertainties of the measured quantities. Standard orthogonal uncertainties are reported in Table II.

B. High-stress results

For high-stress experiments, shorter laser-pulse durations and unloading at the drive surface typically produced shocks that decayed in amplitude with time.[31,34,42,45] Time-integrated measurements (e.g., shock-travel times), often provided insufficient constraints on the shock conditions present during the experiment. For shock stresses above ~600 GPa, the shock front in diamond was reflecting,[31] permitting time-resolved velocimetry of the decaying shock as it transited the diamond.[31,34,42,45] In some experiments the shock was initially reflecting but became nonreflecting during transit.[31]

For experiments where the shock remained reflecting throughout transit (Figs. 9 and 10), it was possible to measure shock velocity immediately before arrival at the free surface. Then, immediately after arrival, the free-surface velocity could be measured. The shock at the free surface exhibited either single- or two-wave structure.

The two-wave structure in this type of experiment was interpreted to consist of a transparent, nonreflecting precursor (consistent with observations at low stress) and a reflecting second wave, such that D_2 was measured through the precursor by VISAR interferometry. This could alter χ from that expected for a single, reflecting wave ($\chi=n_0$),[31,42] where n_0 is the ambient index of refraction. Making the index-of-refraction corrections,[58] we obtain for a two-wave (transparent first wave, reflecting second wave) structure

$$\chi = n_0[1 - (1 - n_1/n_0)(1 - D_1/D_2)], \tag{5}$$

where n_1 is the index of refraction behind the first wave. The two terms in parenthesis are small because $D_1\approx D_2$ at conditions where the second shock is reflecting and $n_1\approx n_0$ for any reasonable change in the index of refraction of diamond in the precursor wave. Thus, $\chi=n_0$ is accurate for all reflecting shocks in diamond.

Immediately before and after free-surface arrival of the shock(s), it is reasonable to approximate conditions as those of steady loading. That is, on a time scale short relative to the time scale of shock decay, unsteady loading effects can be ignored and steady-wave analysis (e.g., impedance matching) can be used. In this interval three measurements constrain the state of the shock(s) immediately before free-surface arrival: D_2, u_{f1} (if observed), and u_{f2}. First shock conditions, when visible, were obtained by assuming $u_{f1}=2u_1$ as at low stress, and estimating D_1 (Table II). Inelastic shock conditions were obtained from measurement of D_2 immediately before free-surface arrival and u_{f2} after free-surface arrival, assuming $u_{f2}=2u_2$ (justified by the relatively good agreement of our results, using this assumption, with independent Hugoniot measurements at high stress: Fig. 11).

TABLE II. Experimental results. Uncertainties are in parenthesis and are intended to represent 68.3% (1-sigma) confidence. For stacked diamonds, the sample thickness is the total thickness. Shots beginning with "dh" were conducted at LLNL; numbered shots were conducted at LLE.

Shot	Orientation and configuration	Intensity (10^{16} W/m^2)	Duration (ns)	Drive	Thickness (μm)	D_1 (km/s)	u_{f1} (km/s)	u_1 (km/s)	P_1 (GPa)	ρ_1 (g/cm^3)	D_2 (km/s)	u_{f2} (km/s)	u_2 (km/s)	P_2 (GPa)	ρ_2 (g/cm^3)	D_Q (km/s)
dh6[a]	⟨110⟩	2.50	6	steady	99.1	20.72	2.21	1.107	80.7	3.713	10.8	2.43	1.78	105	3.99	6.95
	single				(1.0)	(0.68)	(0.14)	(0.071)	(5.8)	(0.015)	(1.5)	(0.10)	(0.57)	(20)	(0.26)	(0.98)
dh10[a]	⟨110⟩	5.90	6	steady	207.9	19.90	2.45	1.223	85.5	3.745	12.71	⋯ [b]	2.87	156	4.37	8.95
	stack				(1.4)	(0.45)	(0.09)	(0.043)	(3.5)	(0.010)	(0.38)		(0.21)	(9)	(0.10)	(0.35)
dh9[a]	⟨100⟩	6.03	6	steady	175.9	20.22	2.26	1.13	80	3.723	13.64	3.96	2.89	162	4.33	9.08
	stack				(1.4)	(0.52)	(0.35)	(0.17)	(12)	(0.034)	(0.39)	(0.14)	(0.22)	(10)	(0.10)	(0.36)
dh13[a]	⟨111⟩	6.28	6	steady	224.0	20.74	1.77	0.88	64.3	3.671	15.12	3.20	2.80	165	4.24	9.03[c]
	single				(1.0)	(0.30)	(0.22)	(0.11)	(7.9)	(0.020)	(0.64)	(0.20)	(0.21)	(11)	(0.08)	(0.36)
dh3[a]	⟨100⟩	6.45	6	steady	83.8	19.29	2.65	1.33	89.8	3.774	13.41	4.75	2.99	166	4.38	9.23
	single				(1.3)	(0.73)	(0.25)	(0.13)	(9.1)	(0.028)	(0.93)	(0.26)	(0.24)	(11)	(0.13)	(0.39)
dh2[a]	⟨100⟩	12.30	6	steady	78.8	19.65	2.80	1.400	96.7	3.785	15.21	7.30	4.38	253	4.83	11.61[c]
	single				(1.3)	(0.80)	(0.10)	(0.050)	(5.2)	(0.016)	(0.81)	(0.30)	(0.38)	(20)	(0.20)	(0.49)
dh8[a]	⟨100⟩	13.18	6	steady	174.7	19.47	3.00	1.50	103	3.808	15.86	7.34	4.32	257	4.74	11.61
	stack				(1.6)	(0.58)	(0.32)	(0.16)	(11)	(0.035)	(0.41)	(0.31)	(0.24)	(13)	(0.11)	(0.32)
dh14[a]	⟨111⟩	12.10	6	steady	201.3	20.75	1.66	0.828	60.4	3.661	16.49	5.31	4.39	265	4.74	11.75
	single				(1.5)	(0.36)	(0.09)	(0.043)	(3.3)	(0.008)	(0.53)	(0.15)	(0.26)	(15)	(0.12)	(0.32)
dh5[a]	⟨110⟩	13.32	6	steady	175.6	20.42	2.57	1.28	92.1	3.751	16.44	6.70	4.42	270	4.73	11.83
	stack				(2.6)	(0.56)	(0.21)	(0.10)	(7.8)	(0.021)	(0.41)	(0.23)	(0.27)	(15)	(0.12)	(0.32)
dh1[a]	⟨110⟩	13.18	6	steady	101.8	19.37	2.61	1.303	88.7	3.768	15.40	7.58	4.76	273	4.99	12.07
	single				(1.3)	(0.61)	(0.14)	(0.068)	(5.4)	(0.016)	(0.64)	(0.20)	(0.29)	(16)	(0.17)	(0.33)
dh12[a]	⟨110⟩	15.88	4	decaying	207.7	20.74	2.79	1.40	102	3.769	16.45	⋯ [d]	4.42	274	4.72	11.87
	stack				(2.2)	(0.53)	(0.26)	(0.13)	(10)	(0.027)	(0.92)		(0.43)	(24)	(0.20)	(0.51)
dh17[a]	⟨111⟩	17.45	4	decaying	232.0	20.81	1.86	0.932	68.2	3.680	16.90	⋯ [d]	5.16	316	5.00	12.75
	single				(1.4)	(0.40)	(0.19)	(0.093)	(6.9)	(0.017)	(0.94)		(0.41)	(25)	(0.23)	(0.53)
dh19[a]	⟨110⟩	54.50	4	decaying	205.6	19.55[e]	3.08	1.54	105.7	3.815	19.8	⋯ [d]	8.32	578	6.08	16.95[c]
	stack				(1.5)	(0.82)	(0.20)	(0.10)	(8.2)	(0.025)	(1.4)		(0.70)	(50)	(0.52)	(0.71)
dh15[a]	⟨111⟩	55.48	4	decaying	169.8	22.43[e]	3.65	1.83	143.9	3.826	20.6	⋯ [d]	8.15	599	5.77	16.99[c]
	single				(1.3)	(0.62)	(0.21)	(0.11)	(9.2)	(0.022)	(1.7)		(0.72)	(53)	(0.49)	(0.71)
dh18[a]	⟨100⟩	56.23	4	decaying	167.3	21.6[e]	3.47	1.733	132	3.821	20.8	⋯ [d]	8.18	602	5.77	17.03
	stack				(1.5)	(1.1)	(0.20)	(0.098)	(10)	(0.025)	(1.8)		(0.70)	(53)	(0.49)	(0.72)
41649[f]	⟨110⟩	184.10	1	decaying	500[g]	20.87[h]	3.40	1.70	125	3.827	⋯ [f]	⋯ [f]	⋯ [f]	⋯ [f]	⋯ [f]	⋯ [f]
	single					(0.64)	(0.40)	(0.20)	(15)	(0.041)						
43633[i]	CVD	396.36	1	decaying	420[g]	21.9[j]	5.19	2.60	200	3.987	20.79	16.70	8.35	617	5.83	⋯ [i]
	single					(1.0)	(0.88)	(0.44)	(35)	(0.094)	(0.32)	(0.90)	(0.45)	(34)	(0.22)	

TABLE II. (*Continued.*)

Shot	Orientation and configuration	Intensity (10^{16} W/m^2)	Duration (ns)	Drive	Thickness (μm)	D_1 (km/s)	u_{f1} (km/s)	u_1 (km/s)	P_1 (GPa)	ρ_1 (g/cm^3)	D_2 (km/s)	u_{f2} (km/s)	u_2 (km/s)	P_2 (GPa)	ρ_2 (g/cm^3)	D_Q (km/s)
29424[i]	⟨110⟩	445.78	1	decaying	450[g,k]	21.5[h]	4.88	2.44	184	3.966	20.10	17.35	8.68	621	6.13	… [i]
	single					(1.4)	(0.47)	(0.24)	(21)	(0.059)	(0.25)	(0.23)	(0.11)	(13)	(0.09)	
42454[i]	⟨110⟩	527.49	1	decaying	500[g]	21.5[h]	5.16	2.58	195	3.993	20.84	19.18	9.59	706	6.48	… [i]
	single					(1.6)	(0.64)	(0.32)	(28)	(0.079)	(0.46)	(0.67)	(0.33)	(29)	(0.23)	
20547[i]	⟨110⟩	47.51	3.5	steady	100[g]	21.6[h]	5.50	2.75	209	4.028	20.60	19.89	9.95	726	6.75	… [i]
	single					(1.7)	(0.28)	(0.14)	(20)	(0.056)	(0.40)	(0.30)	(0.15)	(19)	(0.16)	
43634[i]	CVD	589.97	1	decaying	420[g]	… [l]	… [l]	… [l]	… [l]	… [l]	21.60	20.00	10.00	759	6.55	… [i]
	single										(0.25)	(0.40)	(0.20)	(18)	(0.13)	
20550[i]	⟨110⟩	177.77	1	decaying	100[g]	… [m]	… [m]	… [m]	… [m]	… [m]	23.40	22.50	11.25	925	6.77	… [i]
	single										(0.30)	(0.75)	(0.38)	(33)	(0.22)	
20549[i]	⟨110⟩	217.93	1	decaying	100[g]	… [m]	… [m]	… [m]	… [m]	… [m]	23.30	23.00	11.50	942	6.94	… [i]
	single										(0.35)	(0.75)	(0.38)	(34)	(0.24)	

[a]Inelastic wave conditions obtained by impedance matching with D_2 obtained from diamond transit time.
[b]Free-surface inelastic wave arrival missed.
[c]Quartz shock conditions not observed; estimated from scaling of quartz conditions with laser intensity.
[d]Not reported due to shock decay, u_{f2} does not accurately correspond with u_2 estimated by impedance matching.
[e]Precursor velocities are upper bounds.
[f]Inelastic wave conditions could not be accurately estimated.
[g]Diamond thickness not precisely known.
[h]Estimated from elastic Hugoniot models (finite-strain models and linear fit in D-u) fit to ⟨110⟩ elastic wave data (Ref. 47).
[i]Inelastic wave conditions obtained by assuming $u_{f2}=2u_2$ with D_2 obtained from reflecting shock front.
[j]Estimated from Eq. (6) assuming $D_1=D_C$.
[k]Corrected from Ref. 42.
[l]Precursor just barely overdriven; precursor visible at edge of sample where weaker shocks arrived at free surface.
[m]Precursor overdriven.

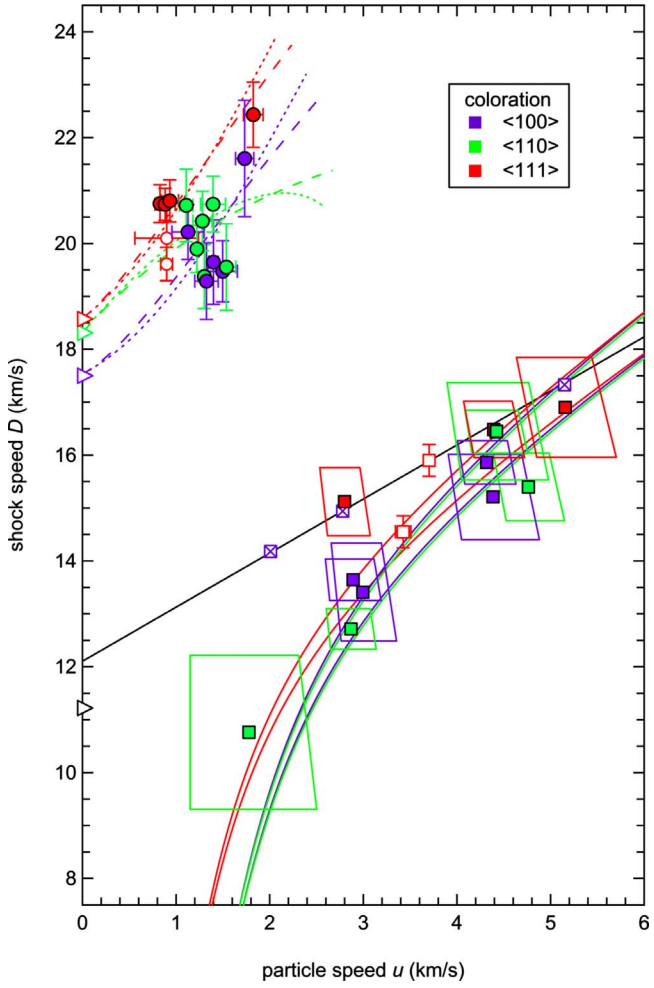

FIG. 7. (Color online) Shock velocity vs particle velocity data for single-crystal diamond. Circles and squares are elastic and inelastic Hugoniot data, respectively. Orientations are ⟨100⟩ (purple), ⟨110⟩ (green), and ⟨111⟩ (red). Filled symbols are present results; two-wave shock data on nearly ⟨111⟩-oriented diamond (Ref. 28) are open circles and squares (red); single-wave shock data on ⟨100⟩ diamond (Ref. 27) are open crossed squares (purple), and a linear fit to this data is the solid black line. Colored solid lines are bounds on the predicted hydrostatic Hugoniot (Appendix B) for each orientation and are observed to be anisotropic at low stress. Colored dashed (dotted) lines are Lagrangian (Eulerian) finite-strain models for the elastic Hugoniots (Ref. 47) centered on the ambient longitudinal sound speeds (colored triangles). Black triangle is ambient bulk sound speed.

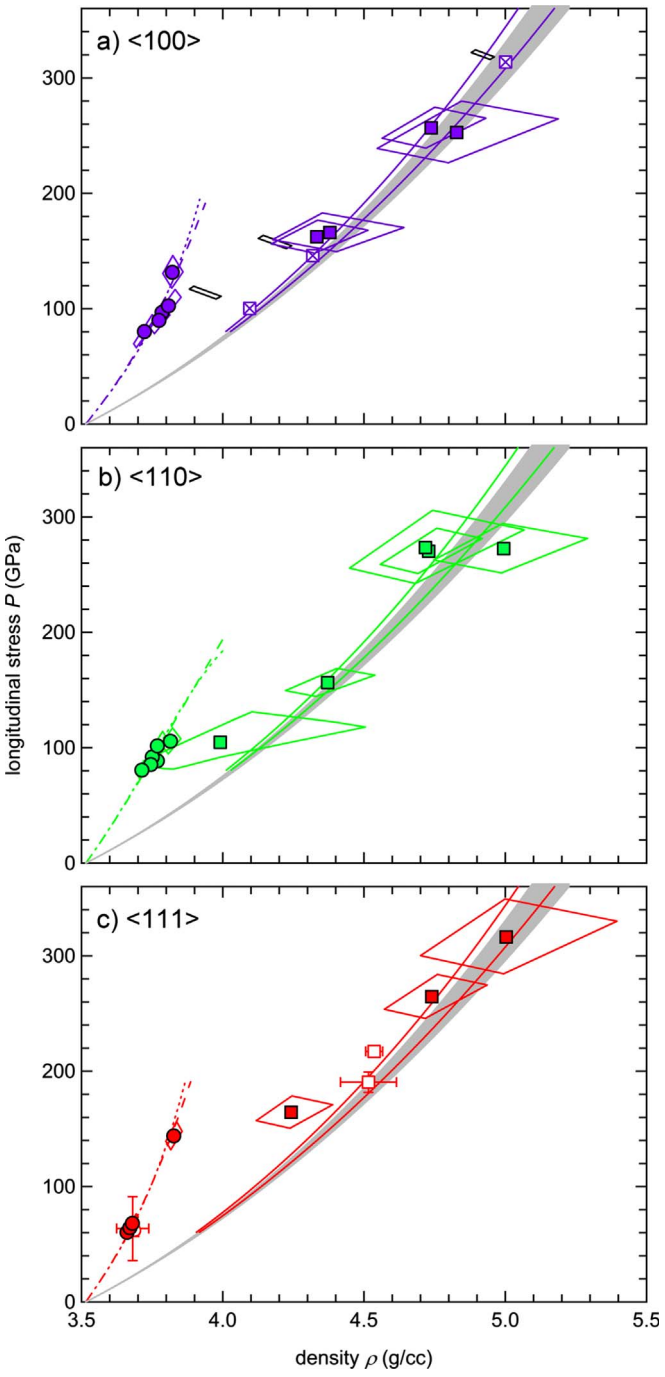

FIG. 8. (Color online) Stress vs density data for (a) ⟨100⟩, (b) ⟨110⟩, and (c) ⟨111⟩ single-crystal diamond. Symbols and coloration are consistent with Fig. 7; circles (squares) are elastic (inelastic) wave data. Present data are filled symbols; data for nearly ⟨111⟩ diamond (Ref. 28) are open symbols; data for ⟨100⟩ diamond (Ref. 27) are crossed open squares, shown with estimated corrections to these datapoints for a two wave structure (Ref. 47) (adjacent, open black polygons). Solid gray region is the hydrostatic isentrope of diamond and its uncertainty (Appendix B). The hydrostatic Hugoniot prediction (bounded by colored solid lines) is virtually identical in each orientation; note however that it is defined only above the HEL. Colored dashed (dotted) lines are Lagrangian (Eulerian) finite-strain models for the elastic Hugoniots (Ref. 47).

Stress and density were then determined through Eqs. (2) and (3).

Our approach amounts to impedance matching in a small spatial region around the interface between two materials (diamond and vacuum, in the present case) during the short time interval that steady loading is a reasonable approximation.[33,34,59,60] For a two-wave structure, wave-amplitude variations during the interval between wave arrivals are accounted for. A high-stress experiment (shot 20547) with approximately steady loading confirmed that there is no resolvable difference between data obtained under nearly steady and decaying loading conditions.

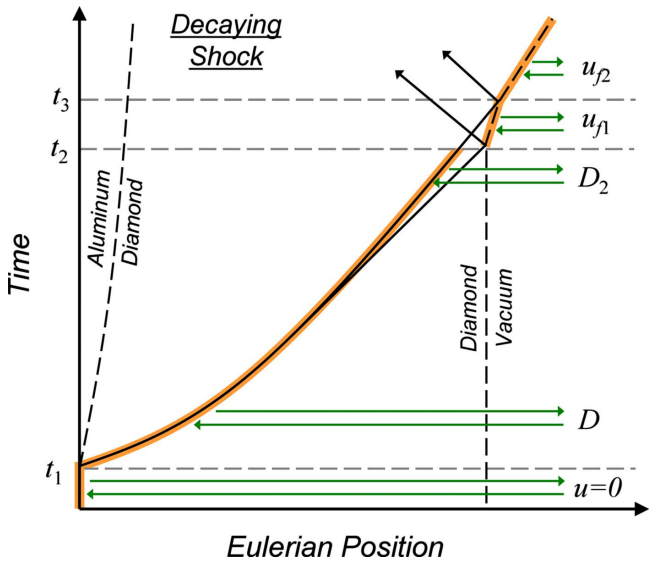

FIG. 9. (Color online) Position vs time diagram for a decaying shock experiment (Fig. 10). Lines, coloration, and time marker numbering are the same as in Fig. 2. Continuous rarefaction from the left is presumed; rightward-propagating rarefactions are not shown. The shock velocity in the single-wave regime, before the shock has split into two waves between t_1 and t_2, is labeled D. Splitting is presumed to occur when a critical velocity (D_C) is reached during decay.

It was observed that with increasing D_2 (near the free surface), the interval between arrivals of the first and second waves decreased until at a critical velocity D_C and above, only a single wave arrival was observed. It is interpreted that below D_C, the precursor is fast enough to separate from the inelastic shock while above it, the precursor is overdriven. Then, for some experiments (e.g., Figs. 9 and 10), D_C was reached as the decaying shock transited the diamond, causing the wave to split before reaching the free surface; in others, D_C was not reached during decay and only a single wave was present during the experiment.

For ⟨110⟩ diamond, D_C lies between ~20.8 and ~23.3 km/s, given the experiments that bound this transition in our data. We can more precisely estimate D_C by considering the distance-time diagram in Fig. 9. Considering the decay of the second shock, observed to be linear in time t late in the experiments (e.g., Fig. 10) as $D_2(t) \equiv D_0\text{-}Rt$, where D_0 and R are constants fit to the data, and assuming the first wave has a constant velocity of $D_1 = D_C$, we have

$$D_C = D_0 - Rt_2 + \sqrt{2R(t_3 - t_2)(D_0 - u_{f1}) - R^2(t_3^2 - t_2^2)}. \quad (6)$$

Equation (6) was used with decaying-shock experiments 29424 and 42454 to give $D_C = 22.3 \pm 0.3$ for ⟨110⟩ diamond. This result is consistent with the splitting of the shock during sample transit; e.g., in Fig. 10, the two-wave structure should be present for only ~4 ns preceding shock arrival at the free surface. If the amplitude of the first wave decreased with propagation distance (due to stress relaxation) rather than remaining constant with $D_1 = D_C$, the value of D_C obtained through Eq. (6) is a lower bound. However, the present measurements and finite-strain predictions[47] suggest that D_1 does not vary much with elastic wave amplitude in ⟨110⟩ diamond and thus Eq. (6) should be accurate. Indeed, the D_1 inferred for the above shots from elastic Hugoniot models (Table II) are in agreement with the independently determined D_C. For the polycrystalline material, a single experiment (43634) occurred right at the overdrive point, constraining D_C to be 21.6 ± 0.3 km/s. The data set in this case showed only a single-wave free-surface arrival at the center of the sample,

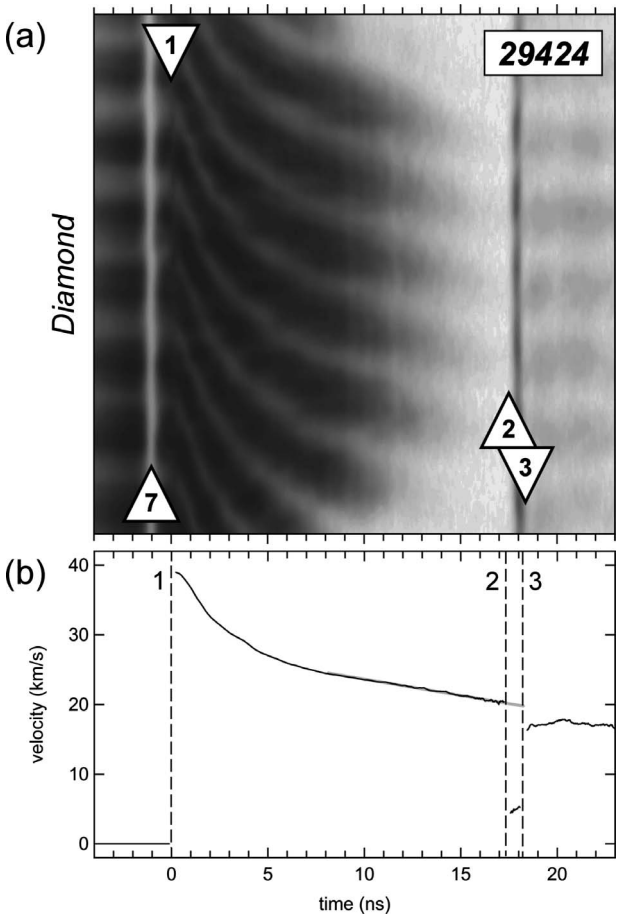

FIG. 10. Line VISAR record (a) for decaying, reflecting shock experiment (shot 29424) and interpreted velocities (b) used for characterizing the two-wave structure of diamond at high stress. The vertical (spatial) axis in (a) is 200 μm full scale and shows the region of planar shock compression in a single diamond sample. Events 1, 2, and 3 are numbered as in Figs. 2, 3, and 9; event 7 is a brief period of opacity in the diamond caused by photoionization during the laser pulse (Ref. 42). At event 1, a strongly reflecting shock appears in the diamond ($\Delta\phi > 0$ and $\phi > 0$); shock velocity then decreases continuously with time as does shock reflectivity as the shock nears the free surface (Ref. 31). At event 2, the free-surface reflectivity, initially eliminated with an AR coating, increases on first-shock arrival, permitting observation of the subsequent free-surface velocity but obscuring the weakly reflecting second shock still within the diamond ($\Delta\phi < 0$ and $\phi > 0$). At event 3, the second shock arrives at the free surface ($\Delta\phi > 0$ and $\phi > 0$). Prior to event 2, we interpret that the reflecting second wave is observed through a transparent first wave. The gray solid line in (b) is a fit to the linear-decay portion of the second shock, extrapolated to estimate shock conditions between events 2 and 3. For (a), the apparent VPF is 15.96 km/s per fringe shift.

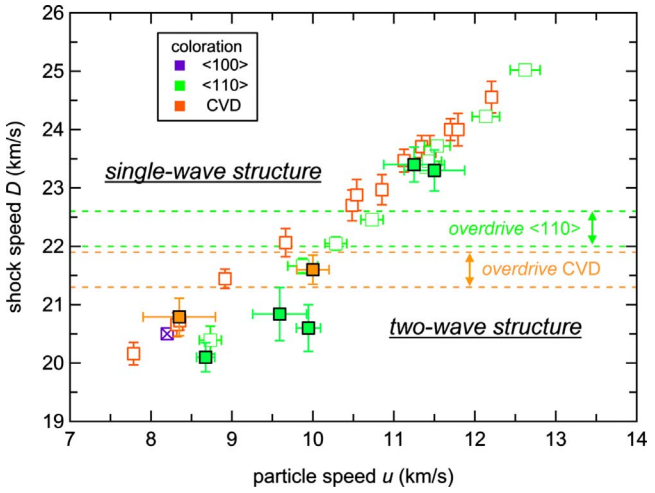

FIG. 11. (Color online) Shock vs particle velocity measurements for diamond at high stress, showing the limit of the two-wave structure. Data obtained using the methods described in Sec. III B are shown as filled squares (⟨110⟩ diamond, green; polycrystalline CVD diamond, orange); in the two-wave regime, only D_2-u_2 data are shown; and corresponding precursor amplitudes can be found in Table II. Dashed colored lines are bounds on the overdrive velocity (D_C) that separates the two-wave and single-wave regimes in the present measurements. Previous high-precision, single-wave Hugoniot data on ⟨110⟩ diamond (Ref. 34) (green open squares), ⟨100⟩ diamond (Ref. 27) (purple crossed square), and polycrystalline diamond (Ref. 35) (orange open squares) are also plotted.

where the main shock was the strongest, and a two-wave arrival toward the edge of the sample, where slightly weaker shocks arrived at the free surface. D_C was also estimated for the polycrystal from Eq. (6) and shot 43633, giving a value consistent with that shown above. It should be noted that D_C is known independently from the Hugoniot.

IV. DISCUSSION

A. Elastic-wave behavior

Elastic precursor amplitudes are found to increase with second-wave (peak) stress, reaching values as high as ~200 GPa before being overdriven. This, together with the decreasing particle velocity behind the precursor wavefront and the decrease in precursor velocity with propagation distance are common phenomena[14,15,22,50,61] that can be interpreted in terms of time-dependant inelastic relaxation of initially-elastic uniaxial strain.[16,17,49,51] Our elastic precursor stresses in ⟨110⟩- and ⟨111⟩-oriented diamond compare well with those measured previously in ⟨110⟩- (Ref. 30) and nearly ⟨111⟩-oriented (Ref. 28) diamond, respectively, at similar peak stresses.

We took the HELs of diamond to be best represented by the weakest elastic precursor observed in each orientation, giving 80.1 (±12.4), 80.7 (±5.8), and 60.4 (±3.3) for the ⟨100⟩, ⟨110⟩, and ⟨111⟩ orientations, respectively. Our rationale is that as precursor stress scales with peak stress, there is a point at which the peak stress is no larger than the precursor stress, such that $P_1 = P_2$; this is the minimum shock stress required to initiate yielding in the form of a second, inelastic shock (the HEL). In each orientation, this stress was estimated from the observed scaling of P_1 with P_2 and corresponded with the weakest precursor stress. Precursor stresses in diamond can thus exceed the HEL by more than a factor of two.

We have observed that elastic precursors in diamond can persist to peak stresses of ~800 GPa in ⟨110⟩-oriented diamond and ~700 GPa in polycrystalline diamond. The limit of the two-wave structure was not observed for the ⟨100⟩ and ⟨111⟩ single-crystal orientations; however, given that elastic-shock velocities in these orientations are similar to or faster than those in ⟨110⟩ (Fig. 7), it is probable that the overdrive stresses and velocities will be comparable to or higher than observed for ⟨110⟩. This shows that, for any orientation of single-crystal diamond and at least one variety of polycrystal, a two-wave structure can occur for shock compression to all states on the solid Hugoniot; and, given the observation of reflecting shocks behind the elastic precursor waves, also to partially molten states on the solid-liquid coexistence curve.[31] The D_C obtained here should be considered upper bounds for experiments in which steady loading conditions are achieved.

B. Inelastic-wave behavior

The most precise inelastic Hugoniot data on single-crystal diamond in the present study, at $P_2 \sim 160$ GPa (Fig. 8), reveals that peak compression states are consistent with hydrostatic stress for the ⟨100⟩ and ⟨110⟩ orientations and inconsistent with hydrostatic stress for the ⟨111⟩ orientation. Our observations are consistent with the expectation that shock-compressed states will either fall on the hydrostatic compression curve or at higher P or D (for given ρ or u) due to strength effects. For P_2 between 200 and 600 GPa, the present Hugoniot data are all compatible with the hydrostatic response although uncertainties in the data and hydrostat are large.

V. THE STRENGTH OF DIAMOND

A. Definitions of strength

The von Mises criterion relates yield strength Y to deviatoric stress σ'_{ij} by

$$Y = (3/2)^{1/2}(\sigma'_{ij}\sigma'_{ij})^{1/2}, \tag{7}$$

where

$$\sigma'_{ij} \equiv \sigma_{ij} - \bar{P}\delta_{ij} \tag{8}$$

for stress tensor σ_{ij} (taken to be positive on compression), δ_{ij} being the Kronecker delta and $\bar{P} \equiv \sigma_{ii}/3$ the mean stress (repeated subscripts imply summation). For a coordinate system aligned with directions of principal stress, such that $\sigma_{11} = \sigma_S$ is the longitudinal shock stress and σ_{22} and σ_{33} are principal stresses transverse to the shock propagation direction, the von Mises criterion reduces to

$$Y = \sigma_S - \sigma_T^Y, \tag{9}$$

where $\sigma_T^Y \equiv (\sigma_{22} + \sigma_{33})/2$. Equation (9) is exact for isotropic lateral stress ($\sigma_{22} = \sigma_{33}$) as is the case for ⟨100⟩ and ⟨111⟩

uniaxial strain in cubic crystals.[62] When lateral stress is anisotropic ($\sigma_{22} \neq \sigma_{33}$) as can be the case for ⟨110⟩ uniaxial strain,[62] Eq. (9) is accurate to within 0.3% for diamond.[47]

For single crystals, strength can also be described using the resolved shear stress on preferred slip planes at yielding.[16,62,63] In diamond, slip and fracture occurs primarily on {111} planes, as expected theoretically[7] and observed in indentation tests,[26] diamond-anvil cell (DAC) (quasistatic) high-pressure experiments,[8] and shock compression.[64] This suggests that finite-strain, while altering crystal symmetry, does not change the preferred slip plane referenced to the unstrained lattice. For elastic uniaxial strain in the ⟨100⟩, ⟨110⟩, and ⟨111⟩ directions of an fcc lattice, and presuming slip occurs on {111} planes in the direction of maximum resolved shear stress (a ⟨112⟩ direction in all cases), the critical-resolved shear stress τ_{CRSS} can be written as

$$\tau_{CRSS} = (\sigma_S - \sigma_T^{CRSS})\cos(\theta_n)\sin(\theta_n), \tag{10}$$

where σ_T^{CRSS} is the transverse stress in the plane containing the shock-propagation direction and the ⟨112⟩ slip direction, and θ_n is the angle from the shock-propagation direction to the {111} slip-plane normal. For ⟨100⟩ and ⟨110⟩ uniaxial strain, $\sigma_T^{CRSS} = \sigma_{22} = \sigma_{33}$; for ⟨110⟩, σ_T^{CRSS} equals either σ_{22} or σ_{33} depending on the coordinates used to define the principal stresses. If slip occurs in a preferred direction that is not ⟨112⟩, then τ_{CRSS} is reduced by the cosine of the angle between ⟨112⟩ and the preferred slip direction in the {111} plane (e.g., if ⟨110⟩ {111} slip is assumed, τ_{CRSS} is reduced by ~13%). The normal (confining) stress on the slip plane at yielding, σ_n, can be written as

$$\sigma_n = \sigma_S \cos^2(\theta_n) + \sigma_T^{CRSS} \sin^2(\theta_n). \tag{11}$$

In the present discussion, crystallographic directions and planes in strained conditions are referenced to their unstrained cubic coordinates.

While the critical-resolved shear stress is arguably a more fundamental measure of strength for single crystals than the yield strength, it has limited applicability because it is not possible to unambiguously define slip-system orientations relative to the stress field once inelastic deformation occurs. Therefore, only the von Mises criterion is used to evaluate strength for states beyond yielding.

To evaluate Y, τ_{CRSS} and σ_n in the shock-compressed states, the lateral stresses σ_T^Y and σ_T^{CRSS} must be determined. One approach, valid for elastic strain and hence only for conditions of incipient yielding at the HEL, is to calculate the stress field σ_{ij} under uniaxial strain using known elastic constants. This method has been described for shock compression of fcc single-crystals with {111} slip systems assuming linear elasticity and infinitesimal strain.[62] Here, because of the high compressions experienced in diamond at its HEL, it was necessary to account for nonlinear elasticity and the change in crystal symmetry under uniaxial strain. In predicting σ_{ij} with nonlinear elastic theory, we have considered elastic constants up to the third order[52,65] using both Lagrangian[16,23,29,47] and Eulerian[47] finite-strain formulations.

The other, more general approach to calculating lateral stress, also applicable for states beyond the HEL, is to compare the measured σ_S with the hydrostatic pressure P_H at a given volume.[13] Considering the definition of $\bar{P}$, we can write

$$\sigma_S - \sigma_T = (3/2)[\sigma_S - \bar{P}]. \tag{12}$$

Equation (12) is valid if $\sigma_T = \sigma_T^Y = \sigma_T^{CRSS}$ when $\sigma_{22} = \sigma_{33}$ (⟨100⟩ and ⟨111⟩ compression) or if $\sigma_T = \sigma_T^Y$ when $\sigma_{22} \neq \sigma_{33}$ (⟨110⟩ compression); when $\sigma_{22} \neq \sigma_{33}$ it is not straightforward to define σ_T^{CRSS} through Eq. (12). At a given volume

$$\bar{P} - P_H \equiv \Delta P. \tag{13}$$

For diamond, $\Delta P = 0$ is a good approximation.[47]

B. Strength of single-crystal diamond

The strength of single-crystal diamond, taken from the measured HEL values in each orientation, is shown in Table III. Equation (12) was evaluated with P_H determined on the hydrostatic isentrope (Appendix B). Also shown in Table III are prior experimental and theoretical strength determinations. The present Y measurements are comparable to those from DAC studies,[8–10] though the DAC determinations tend to be larger. Presently measured Y and τ_{CRSS} are approximately 1/3 of theoretical predictions on compression or shear;[1–6] predictions of strength in tension[4,7] are not directly relevant to our work, as tension promotes a mode of failure with no analog in compression.

It is observed in the present data that τ_{CRSS} depends on loading direction and increases with σ_n (Fig. 12). This is consistent with theoretical expectations.[3,5] The observed increase is approximately linear with a slope of ~0.32, comparable to that predicted by Ref. 3 (~0.26) but significantly larger than predicted by Ref. 5 (~0.07). Analyzing HEL data for silicon[61] (also an fcc lattice) in the same manner as for diamond, a similar dependence of τ_{CRSS} on σ_n is observed (Fig. 12). In contrast, τ_{CRSS} in single-crystal (fcc) copper is independent of σ_n;[62] this may be because the low confining stress at the HEL in copper is not enough to significantly alter that material's strength.

The observation that the strength of single-crystal diamond increases with confining stress may explain the higher yield strengths observed in DAC experiments, as yielding in the DAC occurs at higher confining stress than yielding under shock loading. We note that ramp-compression data on polycrystalline diamond[11] suggest that the elastic strength of single crystal and polycrystalline diamond are comparable under high strain-rate dynamic loading.

C. Yield strength under inelastic compression

The behavior of the yield strength under inelastic compression is shown in Fig. 13. In this figure, the strength observed in the precursor (Y_1) and the strength observed in the inelastic wave (Y_2) are compared using the quantity Y_2/Y_1. Y was determined from Eq. (12) with P_H calculated on the hydrostatic isentrope for Y_1 and the hydrostatic Hugoniot for Y_2 (Appendix B).

For inelastic compression just beyond the HEL (to ~160 GPa) the strength response varies with orientation.

TABLE III. Strength of single-crystal diamond.

Type of study	Y (GPa)	τ_{CRSS} (GPa)	σ_N (GPa)
	Experiment		
⟨100⟩ shock[a]	61 ± 15	29 ± 7[b]	35 ± 11
⟨100⟩ shock[c]	77 ± 12	37 ± 6[b]	31 ± 6
⟨100⟩ DAC[d]	130 ± 10		
⟨110⟩ shock[a]	73 ± 9	33 ± 4[b]	56 ± 7
⟨110⟩ shock[c]	80 ± 8		
⟨110⟩ DAC[e]	94 ± 4		
⟨111⟩ shock[a]	56 ± 10	18 ± 4[b]	12 ± 3
⟨111⟩ shock[c]	61 ± 4	20 ± 2[b]	7 ± 1
⟨111⟩ DAC[f]	81 ± 5		
	Theory		
CRSS[g]		91.6[h]	0
CRSS[i]		121[h]	0
CRSS[j]		95[b]	0
CRSS[k]		93[b]	0
CRSS[l]		96.6[b]	0
CRSS[j]		108[b]	50
CRSS[l]		101[b]	62
⟨100⟩ compression[m]	200		
⟨100⟩ tension[n]	225		
⟨110⟩ tension[n]	130		
⟨111⟩ tension[n]	90		
⟨111⟩ tension[k]	95		

[a]This study, calculated from finite-strain models.
[b]⟨112⟩ {111} slip system considered.
[c]This study, calculated from Eq. (12).
[d]Reference 8.
[e]Reference 10, lower bound.
[f]Reference 9, lower bound.
[g]Reference 1.
[h]⟨110⟩ {111} slip system considered.
[i]Reference 2.
[j]Reference 3.
[k]Reference 4.
[l]Reference 5, Fig. 3(c).
[m]Reference 6.
[n]Reference 7.

The ⟨111⟩ orientation exhibits nearly elastic-plastic compression with no resolvable change in strength whereas the ⟨100⟩ and ⟨110⟩ orientations show a significant loss of strength and, in the case of ⟨110⟩ compression, nearly hydrostatic postshock stress. At higher stresses (above 200 GPa), the strength behavior is not as well resolved (due to larger uncertainties in the data and hydrostat) but the results remain consistent with a significant loss of strength in some orientations.

The differences in the strength response appear to be reflected in the structure of the free-surface wave profiles (Fig. 4), which, at ~250 GPa, have documented distinct elastic reverberation features in the ⟨100⟩ and ⟨110⟩ data, and a lack

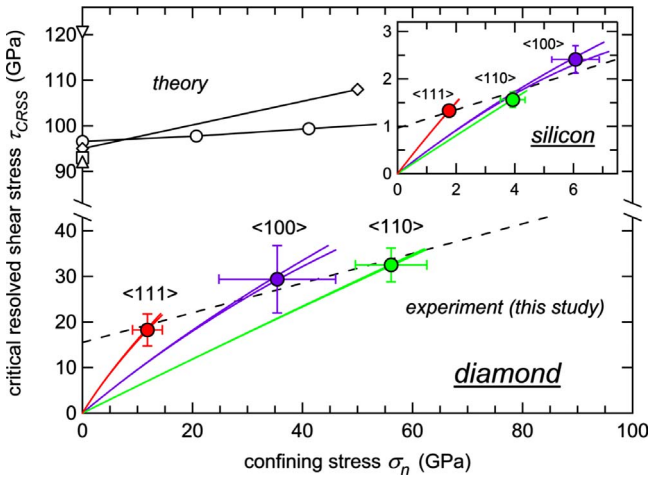

FIG. 12. (Color online) Critical-resolved shear stress vs confining stress. Data for diamond (colored filled circles) were obtained from finite-strain models (Table III) and a linear fit to the data (dashed black line) represents the elastic limit. Solid colored lines show finite-strain predictions (Eulerian and Lagrangian) of stress evolution prior to intersection with the elastic limit. Theoretical studies for diamond are black open symbols: Ref. 1 (upward triangle), Ref. 2 (downward triangle), Ref. 4 (square), Ref. 3 (diamonds connected by solid line), and Ref. 5, Fig. 3(c) (circles connected by solid line). Inset: HEL data on silicon from Ref. 61 analyzed in the same manner as diamond ({111} slip assumed) and plotted with identical symbols; nonlinear elastic constants for Si taken from Ref. 74.

of this feature in the ⟨111⟩ data. Considering that the elastic reverberation wave should be initially quasidiscontinuous, the sharp reverberation feature in the ⟨100⟩ and ⟨110⟩ data is consistent with reverberation against an inelastic shock of short rise time whereas the lack of this feature in ⟨111⟩ data indicates reverberation against an inelastic shock of longer rise time. The short rise time of ⟨100⟩ and ⟨110⟩ inelastic

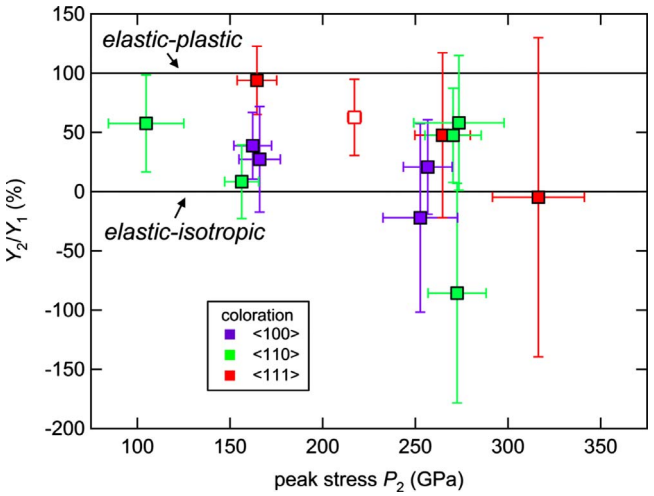

FIG. 13. (Color online) Behavior of strength in the inelastic wave for the present data (colored filled squares) and for the most precise data point of Ref. 28 (open red square). The upper and lower black lines are ideal elastic-plastic and elastic-isotropic strength behavior, respectively.

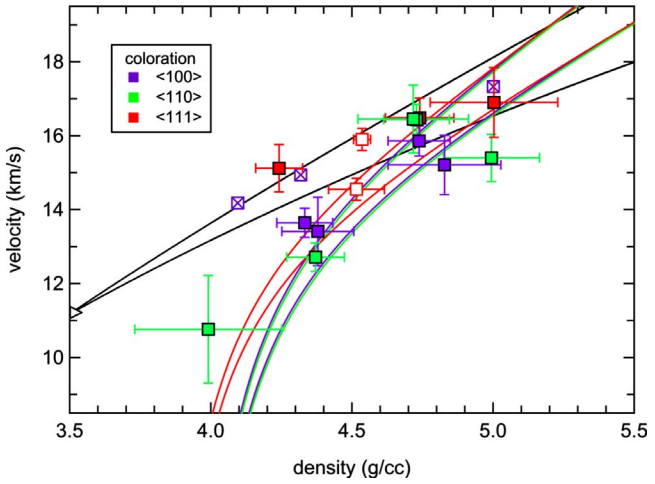

FIG. 14. (Color online) Comparison of inelastic shock velocity with bulk sound velocity. Inelastic shock data are from the present study (colored filled squares), Ref. 28 (open squares), and Ref. 27 (open crossed squares). The black solid lines are limits on the local bulk sound speed (Appendix B); the ambient bulk sound speed is the black open triangle. Colored lines are bounds on shock velocities for elastic-isotropic compression.

shocks is likely coupled to strength loss since the probable mechanism for strength loss—shear banding—would coincide with rapid stress relaxation in the inelastic shock and a sharper wavefront.[18] The long rise time of the ⟨111⟩ inelastic shock suggests slow stress relaxation, likely a consequence of plastic (rather than catastrophic) inelastic deformation and is consistent with the observed retention of strength in this orientation. The differences in the strength response are also reflected in the slow second-shock velocities in the ⟨100⟩ and ⟨110⟩ orientations, relative to local bulk sound speeds (Fig. 14), a common indicator of strength loss.[14,15,19]

The cause of the observed differences in the inelastic strength response is not known but may be related to the significantly lower elastic limit in the ⟨111⟩ orientation. We note that previous data on nearly ⟨111⟩-oriented diamond, which exhibited a low elastic limit and evidence for nonhydrostatic stress under shock compression (Fig. 8), are consistent with the present ⟨111⟩ data.

Finally, the observation that limiting free-surface release velocities are low ($u_{f2} < 2u_2$) at $P_2 < 300$ GPa for all orientations shows that strength can affect the unloading behavior of diamond even in cases where it has been significantly reduced on initial shock compression.[66] This is consistent with the idea of a transient strength-loss mechanism, such as shear banding during shock compression followed by postshock hardening due to the dissipation of thermal heterogeneities.[15,17,18,20]

D. Impurity effects

The preceding discussion treats the dynamic strength of single-crystal diamond as if it were independent of diamond type. However, under quasistatic loading, the presence of impurities is known to affect the mechanical properties of diamond[26] and it is reasonable to expect similar effects under dynamic loading. Type Ib diamonds, used here to study the ⟨111⟩ orientation, feature dispersed substitutional nitrogen defects, and are known to exhibit low strength in quasistatic indentation experiments, as well as the strongest tendency toward plasticity.[26] In contrast, types Ia and IIa diamonds, used to study the ⟨100⟩ and ⟨110⟩ orientations, typically contain aggregate nitrogen impurities (Ia) or lack significant nitrogen impurities (IIa), and tend to be harder in indentation tests, more resistant to plastic flow, and more prone to fracture in comparison with Ib samples.[26] These properties are consistent with the lower HEL and tendency to yield plastically of ⟨111⟩-oriented Ib samples and with the higher HELs and loss of strength on yielding apparent in ⟨100⟩- and ⟨110⟩-oriented Ia and IIa samples. Thus, while our strength data on single crystals has been interpreted in the context of crystalline anisotropy, it may become evident through further study that our observations have been influenced by defect content.

VI. COMPARISON TO OTHER HUGONIOT MEASUREMENTS

There have been a number of studies of the shock Hugoniot of diamond in the stress range examined in the present study,[27,28,32–35] though only one of these studies reported a two-wave structure.[28] In this section, we consider the previous Hugoniot data in the context of the present measurements. Since some data in which single waves were reported are more precise than the present work and do not depend on assumptions that may reduce accuracy (i.e., $u_{f2}=2u_2$ used in the present study at $P_2 > 600$ GPa), we examine whether any systematic errors might have been incurred in those experiments where a two-wave structure was likely to have been present but unobserved.

A. Hicks *et al.* 2008

Some of the present authors (Hicks *et al.*,[34] HEA) have recently published diamond Hugoniot measurements from 600 to 1900 GPa on ⟨110⟩-oriented diamond (Fig. 11). The present measurements on this orientation suggest that a two-wave structure should have occurred in diamond in the lowest-stress experiments of that study (at stresses less than ~800 GPa and shock velocities less than 22.3 ± 0.3 km/s). As in Sec. III B of the present work, the velocity of the reflective (inelastic) shock in diamond was measured by VISAR in that study. An elastic precursor, had one been present, would not have affected this measurement or been observable, though it could have generated a systematic error in the analysis. This error is negligible if elastic precursor conditions are presumed similar in HEA and the present work. For the lowest-stress datapoint, where the error is largest, estimated corrections for a two-wave structure are −0.4% in u_2, +0.6% in P_2, and −1.0% in ρ_2, which are well within the uncertainty of the original data.

B. Other data

High-stress diamond Hugoniot data have also been reported by Knudson, Desjarlais, and Dolan[35] (KDD) for

stresses between 550 and 1400 GPa on two varieties of polycrystalline diamond (Fig. 11); single-wave compression was reported. The microcrystalline samples used in that study are derived from the same manufacturing process and supplier as the polycrystalline samples studied here, and are considered to be identical. The present measurements of D_C in this material (21.6 ± 0.3 km/s) indicate that a two-wave structure may have been present at stresses lower than ~700 GPa in the experiments of KDD. It is not clear if an elastic precursor could have been observed in those experiments or how it would have affected the measurements. We note that a significant kink in the KDD Hugoniot at ~21.5 km/s, identified as the onset of melting by those authors, is identical to D_C observed in the present study for microcrystalline diamond. We also note that the Hugoniot data of HEA, KDD, and the present study are in good agreement in the overdriven regime and diverge in the regime of the two-wave structure (Fig. 11).

Lower-precision high-stress Hugoniot data on ⟨100⟩ (Ref. 33) and ⟨110⟩ (Ref. 32) diamond (500–2000 GPa) also reported single waves. The present observations suggest that elastic precursors were likely to have been present in some experiments from these studies as well. This could explain the discrepancy between the travel-time-based and interferometry-based shock velocity measurements in Ref. 33 at low stress, and suggests that the transition identified as melting in that study may also be related to precursor overdrive.

Two prior studies have examined the diamond Hugoniot at stresses below 500 GPa.[27,28] The data of Kondo and Ahrens,[28] which included a two-wave structure and studied stresses of ~200 GPa in nearly ⟨111⟩-oriented diamond, are generally consistent with the present data on ⟨111⟩ diamond (Figs. 7, 8, and 13).

We conclude that the single-wave Hugoniot data of Pavlovskii[27] on ⟨100⟩ diamond at stresses from 100 to 600 GPa are in significant error. This is evident without reference to the present measurements: three out of four datapoints in that study have shock velocities less than the ambient ⟨100⟩ longitudinal sound speed (Fig. 7), guaranteeing the presence of a precursor wave in those experiments. The present data on ⟨100⟩ diamond reinforce this conclusion and suggest that the fourth datapoint may also have exhibited a two-wave structure. Accounting for the two-wave structure reveals substantial systematic error in the original data—as large as 20% in stress and 5% in density or 37% in $\Delta\rho=\rho_2-\rho_0$ for the lowest-stress datapoint.[11,47] While Pavlovskii's original single-wave data are consistent with hydrostatic stress, estimated corrections to this data for the unobserved elastic precursor result in a significant divergence from a hydrostatic response (Fig. 8).

VII. CONCLUSIONS

We observe a two-wave elastic-inelastic shock structure in three orientations of diamond single crystal and at least one variety of diamond polycrystal to peak stresses as high as ~800 GPa. Finite postshock shear stress is observed for compression of ⟨111⟩-oriented diamond (this study) and nearly ⟨111⟩-oriented diamond[28] for shock loading to hundreds of GPa. Theoretical Hugoniot calculations assuming single-wave shock compression and hydrostatic stress conditions[31,35,37,38] thus may not provide accurate representations of the shock Hugoniot.

The low-stress Hugoniot of Pavlovskii[27] is inconsistent with the present results and a general linear D-u description of the diamond Hugoniot does not appear to be realistic due to: (1) the high elastic limit and the wide range of conditions over which the two-wave structure occurs; (2) the occurrence of strength loss beyond the elastic limit (which produces a nonlinear D-u response); (3) variations in the shock response with initial sample properties; and (4) the occurrence of phase transitions[31,35,37,38] at higher stress.

There is good agreement between the most precise Hugoniot data at high stress[34,35] only in the overdriven regime (Fig. 11); in the regime of the two-wave structure these data sets diverge, consistent with our conclusion that strength effects are present and need to be taken into account. The observation of an elastic precursor at conditions where the second shock is reflecting is evidence that the two-wave structure can persist into the partially molten shock regime.[31] We find that reported signatures of melting at 700–800 GPa[33,35] are well correlated with observed transitions from two- to single-wave structures and thus could be related to precursor overdrive. The onset of reflecting shocks[31]—occurring at ~600 GPa in ⟨110⟩ diamond[34]—suggests that melting can begin at lower stress. Recent shock-temperature measurements also support an initiation of melting at ~600 GPa (in both polycrystalline and ⟨110⟩ diamond).[36] This stress is near the lower end of theoretical predictions for the onset of melting which range from 625–745 GPa when single-wave compression is assumed.[35,37,38] Hugoniot predictions including the two-wave structure will be warmer (Appendix B) and are thus likely to intersect the melting curve at lower stress.

ACKNOWLEDGMENTS

Much of this research was completed at the University of California, Berkeley (Ref. 47). The authors thank Marcus Knudson, Yogendra Gupta, Michael Winey, Stefan Turneaure, Rudolf Wenk, and Brent Grocholski for helpful discussions; Dwight Price, Ray Smith, Steve Letts, Walter Unites, Gary Loomis, and the staff of the Jupiter and Omega laser facilities for technical support; the SEGRF and ILSA programs at LLNL for financial support; and an anonymous reviewer for comments on the manuscript. This work was performed under the auspices of the U.S. Department of Energy by Lawrence Livermore National Laboratory under Contracts No. W-7405-Eng-48 and No. DE-AC52-07NA27344, and by the University of Rochester under Cooperative Agreement No. DE-FC03-92SF19460.

APPENDIX A: EVALUATION OF DRIVE STEADINESS

The laser-driven shocks used in the present study are inherently unsteady. As the shock travels away from the driven surface, it experiences perturbations in amplitude, both posi-

tive and negative, due to variations in the pressure of the laser-driven plasma during irradiation and due to release following laser shutoff. The latter effect dominates our present experiments at $P_2 > 300$ GPa, causing shock decay with time. For $P_2 < 300$ GPa, approximately steady-loading conditions are achieved with perturbations in shock-front amplitude being both positive and negative but centered about some mean state. It is the mean state which we have attempted to characterize in our experiments as this is expected to reasonably represent a state that would be obtained under ideal steady loading. Below we characterize the magnitude of these perturbations in such optimized, quasisteady experiments, using the quartz window as a diagnostic of loading stability. We note that in such experiments, drive instability should affect primarily second-shock amplitude (in diamond) since the elastic precursor, once separated from the second shock, should be relatively insensitive to its amplitude.

Conditions at the quartz shock front and their variation with time are observed in VISAR and SOP records (e.g., Fig. 3) since the quartz shock front is reflecting and emissive[45] for most of the experiments. The drive-pressure perturbations affecting the shock in quartz can be presumed to similarly affect the shock in diamond. Though the diamond shock is not reflecting, transparent, or emissive at low stress,[31,47] preventing time-resolved study of shock conditions, its variability in time can be estimated from that observed in quartz using the relation

$$t_Q = \left(\frac{c_Q}{c_Q + u_Q - D_Q}\right)\left(\frac{c_D + u_D - D_D}{c_D}\right)t_D, \qquad \text{(A1)}$$

where a given perturbation due to the laser drive arrives at the quartz and diamond shock fronts at time t_Q and t_D, respectively (where t_Q and t_D are measured relative to shock breakout into diamond and quartz). It is assumed in Eq. (A1) that perturbations arrive at the base of the diamond and quartz simultaneously and that they are small enough that constant D, u, and c can be assumed, where c is the sound speed in the shock-compressed state; subscripts "Q" and "D" denote quantities in quartz and diamond, respectively. Accounting for impedance mismatches,[67] variations in shock stress in diamond up to t_D (δP_D) can be estimated from observed variations in quartz up to t_Q (δP_Q) by

$$\frac{1 + Z_A/Z_Q}{1 + Z_A/Z_D}\delta P_Q = \delta P_D, \qquad \text{(A2)}$$

where Z_A, Z_Q, and Z_D are the impedances of aluminum, quartz, and diamond, respectively, and can be estimated from the respective Hugoniots.

In shot dh14, at a mean peak stress of ~265 GPa in diamond and ~180 GPa in quartz—Fig. 3(a)—VISAR observation of the quartz shock front revealed variations in shock velocity with time. Equation (A1) gives $t_Q \sim 0.92\ t_D$ for this experiment with D and u measured in the experiment (Table II), c_Q (~14 km/s) estimated from measured sound speeds in molten quartz,[68] and c_D (~26 km/s) estimated as a longitudinal sound speed $c_D = c_B\sqrt{3(1-\nu)/(1+\nu)}$ from the Poisson ratio $\nu \sim 0.1$ (Ref. 26) and the bulk sound speed c_B (Appendix B). Thus, drive-stress perturbations affecting the diamond shock front to $t_D \sim 12$ ns (the time it takes for the second shock to transit the diamond) have similarly affected the quartz shock front to $t_Q \sim 11$ ns (a time at which the quartz shock is still transiting the sample). The directly observed variation in the quartz shock-front conditions to $t_Q \sim 11$ ns has a standard deviation of $\pm 2.5\%$ in shock velocity and $\pm 6.4\%$ in stress. Estimating $Z_A \sim 56$, $Z_Q \sim 52$, and $Z_D \sim 75$ GPa/(km/s) at the appropriate high-stress conditions, a $\pm 7.6\%$ variation in stress at the diamond shock front during sample transit is estimated; this is roughly equivalent to the uncertainty in P_2 for this experiment, showing that the effects of unsteady loading are accounted for in our uncertainty.

Thermal emission variations in quartz were consistent with the variations in shock velocity. In a number of experiments—e.g., Fig. 3(c)—time-resolved velocimetry was not obtained (due to poor AR coatings) and only thermal-emission data was available. By comparison of emission and VISAR data from different experiments, it was clear that loading stability was relatively constant for given laser-drive conditions.

APPENDIX B: HYDROSTATIC HUGONIOT PREDICTION

The Hugoniot of diamond—assuming elastic-isotropic compression (hydrostatic conditions in the peak state)—can be predicted by a thermodynamic pathway that considers isentropic compression to the final volume, V_2, followed by isochoric heating at V_2 to final pressure P_2 and internal energy E_2.[69] In the present treatment we explicitly account for the two-wave structure. The isentropic compression step is described here by a third-order Birch-Murnaghan equation of state, where the subscript S is used to denote isentropic conditions.

$$P_S(f) = 3K_{0S}f(1+2f)^{5/2}[1 + (3/2)(K'_{0S} - 4)f], \qquad \text{(B1)}$$

where $f = (1/2)[(V_0/V)^{2/3} - 1]$ is the Eulerian isotropic strain, $K_{0S} = -V_0(\partial P/\partial V)_{S,P=0}$ is the ambient isentropic bulk modulus, and $K'_{0S} = (\partial K_{0S}/\partial P)_{S,P=0}$ is the pressure derivative of the bulk modulus. Isothermal compression is also described by Eq. (B1) if the isentropic moduli are replaced by isothermal moduli: $K_{0T} = -V_0(\partial P/\partial V)_{T,P=0}$ and $K'_{0T} = (\partial K_{0T}/\partial P)_{T,P=0}$.[70] The isochoric heating step can be described by the Gruneisen equation of state, $\gamma = V(\partial P/\partial E)_V$, where γ is the Gruneisen parameter, leading to

$$P_2(V_2) = P_S(V_2) + (\gamma/V_2)[E_2(V_2) - E_S(V_2)]. \qquad \text{(B2)}$$

The internal energy of the final state E_2 is defined by the Hugoniot equation[22]

$$E_2 - E_0 = \tfrac{1}{2}(P_2 + P_1)(V_1 - V_2) + \tfrac{1}{2}(P_1 + P_0)(V_0 - V_1), \qquad \text{(B3)}$$

which has been adapted for a two-wave system. With Eq. (B3), and considering that $P_S = -(\partial E/\partial V)_S$, Eq. (B2) can be written as

$$P_2(V_2) = \left\{1 - \frac{1}{2}(\gamma/V_2)(V_1 - V_2)\right\}^{-1} \times \left\{P_S(V_2) + \frac{\gamma}{V_2}\left[\frac{P_0(V_0 - V_1)}{2} + \frac{P_1(V_0 - V_2)}{2} + \int_{V_0}^{V_2} P_S dV\right]\right\}. \quad \text{(B4)}$$

The predicted D_2 and u_2 are then determined from $P_2(V_2)$ using Eqs. (2) and (3). In this analysis, the fact that the elastic precursor is in a state of anisotropic stress does not need to be considered explicitly; only the isotropically stressed final state is important.

The thermodynamic parameters required by our model are K_{0S}, K'_{0S}, and γ. In the present model we assume that γ varies as $\gamma = \gamma_0(V/V_0)$, where $\gamma_0 = 0.773$ is the ambient value of γ (though predictions are not significantly different if $\gamma = \gamma_0$ is assumed). A precise value of K_{0S} was obtained from the isentropic second-order elastic constants[52,70] as $K_{0S} = 444.8$ (± 0.7) GPa; this was consistent with but more precise than $K_{0S} = 437.8$ (± 8.5) GPa obtained from isothermal static compression measurements of K_{0T}.[47,71,72] K'_{0S} was determined from K'_{0T} measured by isothermal compression[47,71,72] as $K'_{0S} = 3.93$ (± 0.27).

We consider this model accurate to ~400 GPa; above this stress, uncertainties become large, extrapolations become model dependent,[47] and phase transitions[31,38] may affect the compressibility.

For the calculations of P_2, ρ_2, D_2, and u_2, we considered the parameters of the elastic precursor P_1, ρ_1, D_1, and u_1 to be fixed at the HEL. Uncertainty in the HEL and the scaling of precursor amplitude with second-wave stress are not used in the predictions for the sake of clarity. Accounting for precursor uncertainty and scaling somewhat affects the D_2-u_2 predictions but does not noticeably affect the P_2-ρ_2 predictions.

In the case of single-wave shock compression, i.e., when the elastic precursor is overdriven, $V_1 = V_0$, and $P_1 = P_0$ in Eq. (B4). One effect of considering the precursor is to increase the dissipative thermal pressure $P_{diss} \equiv P_2 - P_S$ at a given volume. At $P_2 \sim 150$ GPa on the hydrostatic Hugoniot, $P_{diss} \sim 5$ GPa for a two-wave treatment, compared to a $P_{diss} \sim 2$ GPa for a treatment that ignores the elastic precursor. The difference in thermal pressure ΔP_{Th} between these two treatments (~3 GPa) is related to the temperature difference ΔT by $\Delta P_{Th} = \gamma_0 \rho_0 C_V \Delta T$, assuming a constant specific heat C_V and the volume dependence of γ discussed earlier. Estimating C_V from its measured value at 1000 K and ambient pressure,[73] the temperature difference between the single- and double-wave calculation at $P_2 \sim 150$ GPa is ~625 K. This is comparable to the calculated single-wave shock temperature of 650–1200 K.[37,38] Thus, at low stresses in diamond, elastic-isotropic compression produces Hugoniot temperatures approximately 50–100 % larger than what would be obtained by single-shock isotropic compression.

The bulk sound speed c_B at V_2 was estimated from Eq. (B1) as $c_B = \sqrt{(\partial P/\partial \rho)_S}$.

*Corresponding author. Present address: Institute for Shock Physics, Washington State University, Pullman, WA 99164, USA. stewartmcwilliams@gmail.com

[1] W. R. Tyson, Philos. Mag. **14**, 925 (1966).
[2] A. Kelly, W. R. Tyson, and A. H. Cottrell, Philos. Mag. **15**, 567 (1967).
[3] H. Chacham and L. Kleinman, Phys. Rev. Lett. **85**, 4904 (2000).
[4] D. Roundy and M. L. Cohen, Phys. Rev. B **64**, 212103 (2001).
[5] Y. Umeno and M. Cerny, Phys. Rev. B **77**, 100101 (2008).
[6] J. J. Zhao, S. Scandolo, J. Kohanoff, G. L. Chiarotti, and E. Tosatti, Appl. Phys. Lett. **75**, 487 (1999).
[7] R. H. Telling, C. J. Pickard, M. C. Payne, and J. E. Field, Phys. Rev. Lett. **84**, 5160 (2000).
[8] M. I. Eremets, I. A. Trojan, P. Gwaze, J. Huth, R. Boehler, and V. D. Blank, Appl. Phys. Lett. **87**, 141902 (2005).
[9] Y. Akahama and H. Kawamura, J. Appl. Phys. **98**, 083523 (2005).
[10] Y. Akahama and H. Kawamura, High Press. Res. **27**, 473 (2007).
[11] D. K. Bradley, J. H. Eggert, R. F. Smith, S. T. Prisbrey, D. G. Hicks, D. G. Braun, J. Biener, A. V. Hamza, R. E. Rudd, and G. W. Collins, Phys. Rev. Lett. **102**, 075503 (2009).
[12] L. V. Altshuler, M. N. Pavlovskii, and V. P. Drakin, Sov. Phys. JETP **25**, 260 (1967).
[13] G. R. Fowles, J. Appl. Phys. **32**, 1475 (1961).
[14] R. A. Graham and W. P. Brooks, J. Phys. Chem. Solids **32**, 2311 (1971).
[15] D. E. Grady, in *High Pressure Research: Applications in Geophysics*, edited by M. H. Manghnani and S. Akimoto (Academic, New York, 1977).
[16] L. Davison and R. A. Graham, Phys. Rep. **55**, 255 (1979).
[17] D. E. Grady, J. Geophys. Res. **85**, 913 (1980).
[18] D. E. Grady and J. R. Asay, J. Appl. Phys. **53**, 7350 (1982).
[19] D. E. Grady, Sandia National Laboratories Report No. SAND94–3266, 1995.
[20] T. J. Vogler and L. C. Chhabildas, Int. J. Impact Eng. **33**, 812 (2006).
[21] J. R. Asay, T. Ao, J. P. Davis, C. Hall, T. J. Vogler, and G. T. Gray, J. Appl. Phys. **103**, 083514 (2008).
[22] J. Wackerle, J. Appl. Phys. **33**, 922 (1962).
[23] R. Fowles, J. Geophys. Res. **72**, 5729 (1967).
[24] T. Mashimo, Y. Hanaoka, and K. Nagayama, J. Appl. Phys. **63**, 327 (1988).
[25] T. Goto, T. Sato, and Y. Syono, Jpn. J. Appl. Phys., Part 2 **21**, L369 (1982).
[26] J. E. Field, *The Properties of Natural and Synthetic Diamond* (Academic, San Diego, 1992).
[27] M. N. Pavlovskii, Sov. Phys. Solid State **13**, 741 (1971).
[28] K. Kondo and T. J. Ahrens, Geophys. Res. Lett. **10**, 281 (1983).
[29] J. M. Boteler and Y. M. Gupta, Phys. Rev. B **66**, 014107 (2002).
[30] M. D. Knudson, J. R. Asay, S. C. Jones, and Y. M. Gupta, Sandia National Laboratories Report No. SAND2001–3738, 2001.
[31] D. K. Bradley, J. H. Eggert, D. G. Hicks, P. M. Celliers, S. J.

Moon, R. C. Cauble, and G. W. Collins, Phys. Rev. Lett. **93**, 195506 (2004).
[32] H. Nagao, K. G. Nakamura, K. Kondo, N. Ozaki, K. Takamatsu, T. Ono, T. Shiota, D. Ichinose, K. A. Tanaka, K. Wakabayashi, K. Okada, M. Yoshida, M. Nakai, K. Nagai, K. Shigemori, T. Sakaiya, and K. Otani, Phys. Plasmas **13**, 052705 (2006).
[33] S. Brygoo, E. Henry, P. Loubeyre, J. Eggert, M. Koenig, B. Loupias, A. Benuzzi-Mounaix, and M. R. Le Gloahec, Nature Mater. **6**, 274 (2007).
[34] D. G. Hicks, T. R. Boehly, P. M. Celliers, D. K. Bradley, J. H. Eggert, R. S. McWilliams, R. Jeanloz, and G. W. Collins, Phys. Rev. B **78**, 174102 (2008).
[35] M. D. Knudson, M. P. Desjarlais, and D. H. Dolan, Science **322**, 1822 (2008).
[36] J. H. Eggert, D. G. Hicks, P. M. Celliers, D. K. Bradley, R. S. McWilliams, R. Jeanloz, J. E. Miller, T. R. Boehly, and G. W. Collins, Nat. Phys. **6**, 40 (2010).
[37] N. A. Romero and W. D. Mattson, Phys. Rev. B **76**, 214113 (2007).
[38] A. A. Correa, L. X. Benedict, D. A. Young, E. Schwegler, and S. A. Bonev, Phys. Rev. B **78**, 024101 (2008).
[39] K. Brugger, J. Appl. Phys. **36**, 759 (1965).
[40] J. M. Winey and Y. M. Gupta, J. Appl. Phys. **96**, 1993 (2004).
[41] L. M. Barker and R. E. Hollenbach, J. Appl. Phys. **43**, 4669 (1972).
[42] P. M. Celliers, D. K. Bradley, G. W. Collins, D. G. Hicks, T. R. Boehly, and W. J. Armstrong, Rev. Sci. Instrum. **75**, 4916 (2004).
[43] J. E. Miller, T. R. Boehly, A. Melchior, D. D. Meyerhofer, P. M. Celliers, J. H. Eggert, D. G. Hicks, C. M. Sorce, J. A. Oertel, and P. M. Emmel, Rev. Sci. Instrum. **78**, 034903 (2007).
[44] D. K. Spaulding, D. G. Hicks, R. F. Smith, J. H. Eggert, R. S. McWilliams, G. W. Collins, and R. Jeanloz, in *Shock Compression of Condensed Matter*, edited by M. Elert *et al.*, AIP Conf. Proc. No. 955, (AIP, New York, 2007), p. 1071.
[45] D. G. Hicks, T. R. Boehly, J. H. Eggert, J. E. Miller, P. M. Celliers, and G. W. Collins, Phys. Rev. Lett. **97**, 025502 (2006).
[46] D. G. Hicks, T. R. Boehly, P. M. Celliers, J. H. Eggert, E. Vianello, D. D. Meyerhofer, and G. W. Collins, Phys. Plasmas **12**, 082702 (2005).
[47] R. S. McWilliams, Ph.D. thesis, University of California Berkeley, 2008.
[48] T. R. Boehly, D. G. Hicks, P. M. Celliers, T. J. B. Collins, R. Earley, J. H. Eggert, D. Jacobs-Perkins, S. J. Moon, E. Vianello, D. D. Meyerhofer, and G. W. Collins, Phys. Plasmas **11**, L49 (2004).
[49] J. W. Taylor, J. Appl. Phys. **36**, 3146 (1965).
[50] J. W. Taylor and M. H. Rice, J. Appl. Phys. **34**, 364 (1963).
[51] J. R. Asay, Y. Gupta, and G. R. Fowles, J. Appl. Phys. **43**, 744 (1972).
[52] R. Vogelgesang, A. K. Ramdas, S. Rodriguez, M. Grimsditch, and T. R. Anthony, Phys. Rev. B **54**, 3989 (1996).
[53] G. R. Fowles, Poulter Laboratories Technical Report No. 003–61, 1961.
[54] T. J. Ahrens, W. H. Gust, and E. B. Royce, J. Appl. Phys. **39**, 4610 (1968).
[55] G. I. Kerley, in *Equations of State for Composite Materials, Kerley Report No. KPS99–4* (Kerley Publishing Services, Albuquerque, NM, 1999).
[56] G. I. Kerley, Int. J. Impact Eng. **5**, 441 (1987).
[57] P. M. Celliers, G. W. Collins, D. G. Hicks, and J. H. Eggert, J. Appl. Phys. **98**, 113529 (2005).
[58] D. Hayes, J. Appl. Phys. **89**, 6484 (2001).
[59] J. Eggert, S. Brygoo, P. Loubeyre, R. S. McWilliams, P. M. Celliers, D. G. Hicks, T. R. Boehly, R. Jeanloz, and G. W. Collins, Phys. Rev. Lett. **100**, 124503 (2008).
[60] D. G. Hicks, T. R. Boehly, P. M. Celliers, J. H. Eggert, S. J. Moon, D. D. Meyerhofer, and G. W. Collins, Phys. Rev. B **79**, 014112 (2009).
[61] W. H. Gust and E. B. Royce, J. Appl. Phys. **42**, 1897 (1971).
[62] O. E. Jones and J. D. Mote, J. Appl. Phys. **40**, 4920 (1969).
[63] W. J. Murri and G. D. Anderson, J. Appl. Phys. **41**, 3521 (1970).
[64] J. H. Eggert, D. G. Hicks, P. M. Celliers, D. K. Bradley, J. E. Cox, W. G. Unites, G. W. Collins, R. S. McWilliams, R. Jeanloz, S. Brygoo, and P. Loubeyre, in *Proceedings of Joint 20th AIRAPT-43th EHPRG International Conference on High Pressure Science and Technology*, Karlsruhe, 2005.
[65] E. Anastassakis, A. Cantarero, and M. Cardona, Phys. Rev. B **41**, 7529 (1990).
[66] R. G. McQueen, S. P. Marsh, J. W. Taylor, J. N. Fritz, and W. J. Carter, in *High-Velocity Impact Phenomena*, edited by R. Kinslow (Academic, New York, 1970).
[67] J. Lipkin and J. R. Asay, J. Appl. Phys. **48**, 182 (1977).
[68] J. A. Akins and T. J. Ahrens, Geophys. Res. Lett. **29**, 1394 (2002).
[69] R. Jeanloz, P. M. Celliers, G. W. Collins, J. H. Eggert, K. K. M. Lee, R. S. McWilliams, S. Brygoo, and P. Loubeyre, Proc. Natl. Acad. Sci. U.S.A. **104**, 9172 (2007).
[70] F. Birch, J. Geophys. Res. **83**, 1257 (1978).
[71] F. Occelli, P. Loubeyre, and R. Letoullec, Nature Mater. **2**, 151 (2003).
[72] F. Datchi, A. Dewaele, Y. Le Godec, and P. Loubeyre, Phys. Rev. B **75**, 214104 (2007).
[73] A. C. Victor, J. Chem. Phys. **36**, 1903 (1962).
[74] H. J. McSkimin and J. P. Andreatch, J. Appl. Phys. **35**, 3312 (1964).